



Drag model of finite-sized particle in turbulent wall-bound flow over sediment bed

Ping Wang¹, Yinghaonan Lei¹, Zhengping Zhu² and Xiaojing Zheng^{2,†}

¹Key Laboratory of Mechanics on Disaster and Environment in Western China, The Ministry of Education of China, Department of Mechanics, Lanzhou University, Lanzhou 730000, PR China

²Research Center for Applied Mechanics, School of Mechano-Electronic Engineering, Xidian University, Xi'an 710071, PR China

(Received 7 May 2022; revised 31 October 2022; accepted 28 February 2023)

Drag force acting on a particle is vital for the accurate simulation of turbulent multiphase flows, but the robust drag model is still an open issue. Fully resolved direct numerical simulation (DNS) with an immersed boundary method is performed to investigate the drag force on saltating particles in wall turbulence over a sediment bed. Results show that, for saltating particles, the drag force along the particle trajectories cannot be estimated accurately by traditional drag models originally developed for an isolated particle that depends on the particle-wall separation distance or local volume fraction in addition to the particle Reynolds number. The errors between the models and DNS are especially clear during the descending phase of the particles. Through simple theoretical analysis and DNS data fitting, we present a corrected factor using the classical, particle Reynolds number dependent drag force model as the benchmark model. The new drag model, which takes the particle vertical velocity into account, can reasonably predict the mean drag force obtained by DNS along a particle trajectory.

Key words: multiphase flow, turbulence simulation, turbulent boundary layers

1. Introduction

Turbulent multiphase flows are common in natural and industrial applications. Examples include aeolian sand storms (Zheng 2009; Pähz et al. 2018; Wang et al. 2019; Zheng, Jin & Wang 2020; Jin, Wang & Zheng 2021; Zheng, Feng & Wang 2021), river sediment transport (Ancy et al. 2008; Seminara 2010; Schmeeckle 2014; Berzi, Jenkins & Valance 2016; Pähz et al. 2020) and fluidized beds (Fortes, Joseph & Lundgren 1987; Grbavcic et al. 1991; Deen et al. 2007; Luo et al. 2016; Esteghamatian et al. 2018), to name a few. In the framework of Euler–Lagrange simulations of particle-laden flows (Li et al.

† Email address for correspondence: xjzheng@xidian.edu.cn

2001; Dritselis & Vlachos 2008; Eaton 2009; Zhao, Andersson & Gillissen 2010, 2013; Capecelatro & Desjardins 2013; Schmeekle 2014; Guan *et al.* 2021; Zheng *et al.* 2021), the quasi-steady drag force is perhaps the most dominant of all the hydrodynamic force contributions (Guan *et al.* 2021). The coupling between the particle and fluid also needs to be realized by adding integral or distributed drag force feedback, among others, into the momentum equation (Rouson 1997; Li *et al.* 2001; Rouson & Eaton 2001; Beetstra, van der Hoef & Kuipers 2007; Dritselis & Vlachos 2008; Eaton 2009; Zhao *et al.* 2013). Even in the Eulerian–Eulerian approach, the coupling terms by averaged equations for momentum also need to be modelled by drag force (Tenneti, Garg & Subramaniam 2011; Chen *et al.* 2020). Therefore, the drag model is vital for the accuracy of simulations and is one of the key issues of turbulent multiphase flow (Balachandar & Eaton 2010). Unfortunately, although many drag models have been proposed under relatively ideal conditions, their applicability for actual turbulent multiphase flow has not been well established so far.

Stokes (1851) first proposed the well-known Stokes drag force $F_D = 3\pi\mu D_p U_\infty$ for a single isolated sphere subject to a steady uniform Stokes flow, where F_D is the drag force, D_p and μ are the particle diameter and dynamic viscosity of the fluid, respectively, and U_∞ is the free-stream velocity usually being used as the particle–fluid slip velocity u_{slip} in practice. This drag model is valid in the limit of $Re_p \rightarrow 0$, with the particle Reynolds number Re_p being defined as $u_{slip} D_p / \nu$, where ν is the kinematic viscosity of the fluid. When the deviation from Stokes flow or the presence of neighbouring particles is considered, the Stokes drag model has to be modified. The correction to the Stokes drag force for $Re_p > 0$ was completed theoretically by Oseen (1910) who proposed a first-order slip-based inertial correction. However, most of the drag correction schemes through theoretical analysis are still limited to $Re_p \rightarrow 0$ in either unbounded models (Hasimoto 1959; Batchelor 1972; Proudman & Pearson 1957; Sangani & Acrivos 1982) or bounded models, including the effect of walls on drag force (Faxén 1922; Vasseur & Cox 1977; Happel & Brenner 1981). Works on a purely theoretical basis are rather difficult for systems in which the volume fraction ϕ_p and particle Reynolds number are non-zero, or more complex influencing factors are involved. For the experiments, measurements based on a pressure drop over packed beds of various materials (Ergun 1952; Epstein 1954; Rumpf & Gupte 1971; Fand *et al.* 1987; Watanabe 1989) are usually used to obtain estimates for the solid particle drag when $\phi_p > 0.1$ and $Re_p > 1$. In addition, some studies also reported particle acceleration and trajectory tracking using non-intrusive measurements such as a high-speed camera, tomographic particle image velocimetry and the shake-the-box method (Ayyalasomayajula *et al.* 2006; Wu *et al.* 2006; Qureshi *et al.* 2008; Schanz, Gesemann & Schröder 2016). However, such experiments provide only indirect information of drag force, and are often not well defined in terms of details such as homogeneity, mobility and so on (Beetstra *et al.* 2007). Most importantly, detailed experimental measurements of particle drag force in an actual multiphase flow, as turbulent two-phase flow over the erodible bed concerned in this paper, are rare and as a result, high-quality data are scarce. In fact, experimental observation is also a great challenge due to particle aggregation and two-phase interaction.

Different from the experimental and analytic methods, particle-resolved direct numerical simulation (PR-DNS) in the framework of body-conforming moving-mesh methods (Feng, Hu & Joseph 1994a,b; Hu, Patankar & Zhu 2001) or immersed boundary methods (IBMs) (Peskin 1977; Uhlmann 2005; Breugem 2012; Luo *et al.* 2019) evaluates the hydrodynamic force on a particle by integrating the pressure and viscous stresses around the particle surface. The exponential growth in computing power over the past

20 years made PR-DNS become a preferred choice for developing more accurate drag correlations over a larger range of ϕ_p , Re_p (Brandt & Coletti 2022) and parameter space. Zeng *et al.* (2009) obtained the hydrodynamic force acting on a finite-sized particle translating parallel to the wall in a stagnant fluid and a stationary particle in a wall-bounded linear shear flow by PR-DNS, based on which a composite drag correlation that is valid for a wide range of $2 < Re_p < 250$ and distance from the wall L was proposed. Lee & Balachandar (2010) furthered this study to a more general case of a translating and rotating particle in a wall-bounded linear shear flow. They provided a composite drag correlation that linearly superposes shear, translational and rotational effects. Ekanayake *et al.* (2020) and Ekanayake, Berry & Harvie (2021) simulated finite-sized particles in both quiescent and linear shear flows with low slip and shear Reynolds numbers. A new drag coefficient correlation that includes higher-order terms in separation distance and the shear-based inertial correction was proposed and tested in a linear shear flow. For the dense flow, the effects of neighbouring particles, through displacing the local fluid, become important and must be accounted for. The fully resolved simulations have also been applied to study the drag force in flow through arrays of structured and random particles (fixed or moving). In this regard, modified drag models need to consider additional parameters, such as the solid volume fraction gradient, superficial velocity gradient (Chen *et al.* 2020), the granular temperature (Zhou & Fan 2014, 2015; Tang, Peters & Kuipers 2016; Huang *et al.* 2017), the particle velocity fluctuation (Luo *et al.* 2021) and so on.

In the turbulent boundary layer, these drag models developed in laminar upstream flows are proven to have limited effectiveness. Zeng *et al.* (2008) simulated isolated finite-sized particles with diameters varying from 3.5 to 25 wall units ($D_p/\eta = 2.0 \sim 14.3$, where η shows the Kolmogorov scale) and located in the buffer region and along the centreplate of channel turbulence. They found that, near the wall, only for small particles (away from the viscous sublayer) under consideration, the instantaneous force is captured well with the standard drag formulation of Schiller & Nauman (1935). Within the buffer layer, the force fluctuation can be correlated well with incoming turbulent flow structures. With increasing particle size, vortex shedding contributes to an increase in drag fluctuation that cannot be captured by the standard drag model. Homann, Bec & Grauer (2013) pointed out that the average drag force increases as a function of the turbulent intensity. This increase is larger than what is predicted by standard drag correlations developed based on laminar upstream flows. Li *et al.* (2019) investigated the forces on a stationary finite-sized particle in wall turbulence over a rough bed and the interaction between the particle and the near-wall turbulent structures. They found that the standard drag formulation with near-wall correction proposed by Zeng *et al.* (2009) can reasonably predict the drag force, provided that the slip velocity is correctly calculated. Again, the large fluctuations due to self-induced vortex shedding probably result in a significant discrepancy. Recently in Li *et al.* (2020), a spherical particle released and suspended in a turbulent open channel flow was tracked by PR-DNS. It is found that the standard drag formulation of Schiller & Nauman (1935) can only reflect the general trend of drag, with the large-amplitude and high-frequency characteristic of the surface forces missed.

In the past two decades a number of PR-DNS investigations of finite-sized particles have also been documented for turbulent two-phase flows. Such studies focused on either turbulence modulation (Pan & Banerjee 1997; Cate *et al.* 2004; Lucci, Ferrante & Elghobashi 2010; Naso & Prosperetti 2010; Yeo *et al.* 2010; Lucci, Ferrante & Elghobashi 2011; Gao, Li & Wang 2013; Tanaka & Teramoto 2015; Schneiders, Meinke

& Schröder 2017; Tanaka 2017; Fornari *et al.* 2019; Yousefi, Ardekani & Brandt 2020) or particle migration (Kidānemariam *et al.* 2013; Kidānemariam & Uhlmann 2014; Lashgari *et al.* 2016, 2017; Kidānemariam & Uhlmann 2017; Ardekani *et al.* 2018; Costa, Brandt & Picano 2020; Yousefi *et al.* 2021). The reader is referred to Brandt & Coletti (2022) for the state-of-the-art progress of particle-laden turbulence. Only a few studies, however, discussed particle forces in turbulent two-phase flows. For example, Esmaily & Horwitz (2018) simulated decaying turbulence laden with inertial particles using point-particle models and compared their results against a particle-resolved simulation. They revealed that the momentum exchange between particles and fluid modifies the slip velocity and produces an erroneous prediction of coupling force. A correction scheme to reduce this error and accurately predict the undisturbed fluid velocity was proposed. Costa *et al.* (2020) simulated a one-way coupled turbulent channel flow laden with small inertial particles. A direct comparison between interface-resolved and drag-force-driven point-particle results was conducted for $\phi_p \sim O(10^{-5})$ and $D_p^+ = D_p u_{\tau,f} / \nu = 3$, where $u_{\tau,f}$ is the friction velocity of particle-free wall turbulence. Ji *et al.* (2013) simulated sediment entrainment on an erodible particle bed in turbulent channel flow. The hydrodynamic forces acting on the particles were presented and the underlying mechanisms of sediment entrainment were discussed.

Despite the numerous studies, as summarized above, particle drag force in multiphase turbulence has not been thoroughly discussed. What are the characteristics of particle drag force in a turbulent multiphase flow and whether previously proposed drag models can predict the drag force acting on particles are still open questions, which inspire the present study. We will simulate turbulent two-phase flow over an erodible particle bed using the PR-DNS method and present an in-depth analysis of the drag force acting on saltating particles. The characteristics of this two-phase flow are: once the fluid velocity or shear velocity is high enough to exceed the threshold condition for the onset of sediment motion, the two-phase flow will come into being with particles suspending, rolling and saltating above the bed. Due to the inhomogeneous nature of wall turbulence in a wall-normal direction and the attenuation of particle concentration along the height, a saltating particle will experience varying local volume fraction, particle-wall separation distance, turbulent velocity fluctuation and mean shear during its descending and ascending phases. As a result, the factors affecting the drag force are quite complex. It is therefore of practical and physical significance to discuss the drag force on particles in such a two-phase flow. The structure of the paper is as follows. In § 2 we introduce the methodology. Dynamic responses of a typical particle during continuous saltations are presented in § 3, together with the validity check of several classical drag models. Then a new drag model is proposed by fitting the simulated results. Finally, we discuss the limits and draw conclusions in §§ 4 and 5, respectively.

2. Numerical methodology

We simulate pressure-driven open channel flow over an erodible particle bed. A Cartesian coordinate system is adopted such that x , y and z denote the streamwise, wall-normal and spanwise direction, respectively. The simulation domain is $[L_x \times L_y \times L_z]/H = 6 \times 1 \times 3$, where H is the half-channel height. The friction Reynolds number based on H , the kinematic viscosity of fluid ν and particle-free friction velocity $u_{\tau,f}$ is $Re_{\tau,f} = u_{\tau,f} H / \nu = 180$. The sediment bed consists of four layers of monodisperse spheres at rest. This quasi-randomly packed particle bed is formed by particles randomly released in the simulation domain that settle under the action of gravity (without hydrodynamic

Drag model of finite-sized particle in wall turbulence

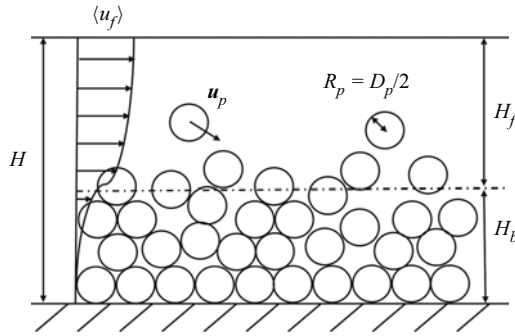


Figure 1. Sketch of the computational set-up. Here $\langle u_f \rangle$ represents the mean velocity of fluid over the streamwise direction, u_p is the velocity of particles, R_p and D_p are the radius and diameter of the particles, respectively, H is the half-channel height, H_b is the effective sediment-bed height and $H_f = H - H_b$.

force) and collision as detailed in Kidanemariam & Uhlmann (2014). The total number of particles is 7200. Figure 1 shows a sketch of the computational set-up, particle bed and moving particles. The particle-to-fluid density ratio is $\rho_p/\rho_f = 2.5$. The particle diameter studied is $D_p/H = 0.1$ and the particle volume fraction is $\phi_{total} = 0.21$, regardless of the particle state of motion. Throughout the paper, subscripts p and f denote particle and fluid phases, respectively. ‘Erodible’ indicates that particles resting on the bed may be entrained by the direct fluid force or by the impact of settling particles. Meanwhile, once a moving particle impacts the bed due to gravity, it may either trap into or rebound from the bed. In this simulation, however, a moving particle can hardly eject other particles resting on the bed due to the low particle-to-fluid density ratio. Shields number, which is defined as $\theta = u_\tau^2/((\rho_p/\rho_f - 1)gD_p)$ and quantizes the mobility of particles, is set to 0.125, where g denotes the gravitational acceleration. The corresponding Galileo number $Ga = \sqrt{(\rho_p/\rho_f - 1)gD_p^3}/\nu$, based on the gravitational velocity scale, is 41.83. We address that the friction velocity u_τ in θ is *a posteriori* determined by evaluating the total shear stress at the height of the mean fluid bed interface H_b . Therefore, particle diameter in such a wall unit is $D_p^+ = D_p u_\tau/\nu = 9.69$.

The numerical methods follow from our previous work in Zhu *et al.* (2022) and Wang *et al.* (2022), and are only briefly introduced here. The flow is incompressible turbulence and governed by the continuity equation and Navier–Stokes equation. Here u_f , v_f and w_f are the streamwise, vertical and spanwise velocities, respectively. A second-order central difference scheme is used for spatial discretization and a second-order Runge–Kutta method is used for fluid time advancement when numerically solving these governing equations. The fractional-step method of Kim & Moin (1985) is applied at each Runge–Kutta substep to ensure that the flow velocity is divergence free. The computational domain is discretized on a uniform Cartesian grid with $N_x \times N_y \times N_z = 540 \times 90 \times 270$. Periodical conditions are imposed in both the streamwise and spanwise directions. No-slip boundary conditions are used on both the bottom wall and sphere surfaces. At the top of the simulation domain, a free-slip condition is applied. The dimensionless time step is $\Delta t_f = 2.5 \times 10^{-4}$ for the fluid solver. The schematic plot of the mean streamwise velocity $\langle u_f \rangle$ is shown in figure 1, where $\langle \cdot \rangle$ represents the ensemble average over the two homogeneous directions x , z and over time. The motion of finite-sized particles is obtained by solving the position, translational velocity and angular velocity in equations expressed,

respectively, as

$$\frac{d\mathbf{x}_p}{dt} = \mathbf{u}_p, \quad (2.1)$$

$$\rho_p V_p \frac{d\mathbf{u}_p}{dt} = \mathbf{F}_h + (\rho_p - \rho_f) V_p \mathbf{g} + \mathbf{F}_c, \quad (2.2)$$

$$\mathbf{I}_p \frac{d\boldsymbol{\omega}_p}{dt} = \mathbf{T}_h + \mathbf{T}_c, \quad (2.3)$$

where V_p and \mathbf{I}_p are the volume and moment of inertia of the spheroidal particle; \mathbf{x}_p , \mathbf{u}_p and $\boldsymbol{\omega}_p$ are the position vector, translational velocity and angular velocity of the particle, respectively; \mathbf{F}_h is the hydrodynamic force tensor; \mathbf{F}_c and \mathbf{T}_c are the collision force and torque acting on the particle, respectively. As in Costa *et al.* (2015), a lubrication model is used for \mathbf{F}_c to consider the short-range interaction when the gap width is smaller than the grid spacing. The collision process between the particles is calculated through a discrete-element model (DEM) based on the soft-sphere approach. An adaptive collision time model (ACTM) (Kempe & Fröhlich 2012; Biegert, Vowinkel & Meiburg 2017) is employed to calculate the collision force. To describe the collision process in the framework of this model, the normal restitution, tangential coefficient and friction coefficient are taken to be $e_{n,d} = 0.97$, $e_{t,d} = 0.39$ and $\mu_c = 0.15$. The dimensionless time step for the particle is $\Delta t_p = \Delta t_f/50$ and the collision time $T_c = 10\Delta t_f$, as in previous studies (Zhu *et al.* 2022). Periodic boundary conditions are applied for particles in the streamwise and spanwise directions. We remark here that particles do not collect at the free surface in this study. The direct-forcing IBM (Uhlmann 2005; Breugem 2012; Kempe & Fröhlich 2012) is used to realize the two-way coupling through adding a localized force term to the incompressible Navier–Stokes equation. The carrier phase is parallelized by the domain decomposition method, while the disperse phase is parallelized by the mirror domain technique (Darmana, Deen & Kuipers 2006) to ensure that each processor stores the same total particle data and the excellent load balance can be achieved. The simulation is run for a total 1.9×10^5 steps ($T^+ = Tu_\tau^2/\nu = 7.8 \times 10^3$) on China’s Tianhe-2 supercomputer at China’s National Supercomputer Center in Guangzhou. In order to reach statistical stability of the two-phase flow, the statistics are sampled during an extra 50 000 steps.

Before presenting the simulated results, we validate the models based on the drafting-kissing-tumbling (DKT) phenomenon of two settling spheres, in addition to the validations performed in Zhu *et al.* (2022). Two spheres of identical diameter and density are first released from rest, and then settle due to gravity. Their initial separation is as small as $|d - D_p|/D_p = 1.0418$, where d is the distance between the centres of the two particles. The leading drafting sphere creates a wake during settling, which attracts and interacts with the trailing sphere by the generated pressure drop in the wake. With the mutual interaction, the two spheres collide with each other (kissing contact) as time evolves that then leads to a significant change in the subsequent trajectory of the two spheres, that is, the trailing sphere catches up to the leading sphere in the vertical direction and overtakes it (tumbling). The DKT phenomenon involves significant processes of sedimentation of a spherical particle in a quiescent fluid and particle–particle collision in a viscous fluid and is a good example for validating the accuracy of PR-DNS. To simulate this case, we set the computational domain and initial positions of the two spheres similar to Breugem (2012) and Luo *et al.* (2019). The properties of the two identical spheres are $D_p = 1.667 \times 10^{-3}$ m and $\rho_p = 1140$ kg m $^{-3}$. The density of the carrying fluid is $\rho_f = 1000$ kg m $^{-3}$.

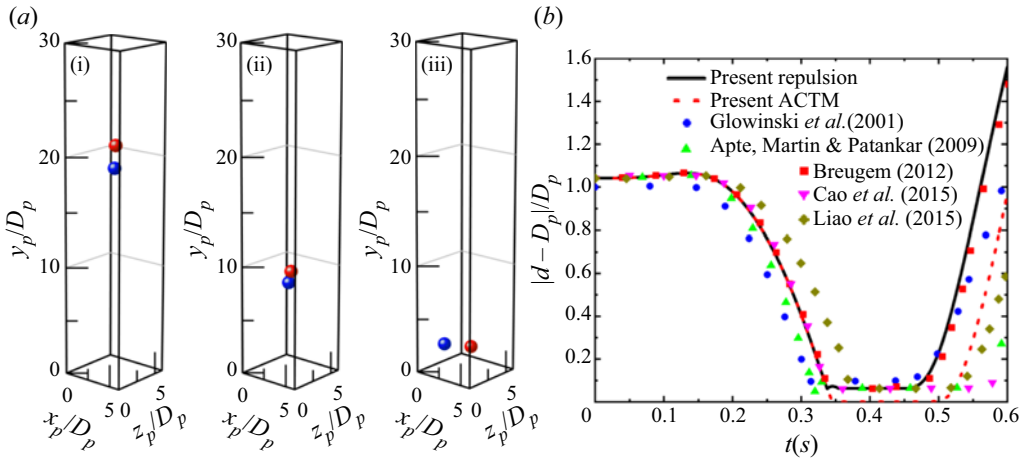


Figure 2. The simulated drafting-kissing-tumbling (DKT) phenomenon. (a i–a iii) Diagrams of the locations of the two spheres at $t = 0.005$ s, $t = 0.391$ s and $t = 0.587$ s, respectively. (b) The gap between two spheres as a function of evolving time.

Figure 2(a) has three side-by-side diagrams showing the position of the two spheres at different times, corresponding to the initial stage ($t = 0.005$ s, figure 2a i), the kissing contact ($t = 0.391$ s, figure 2a ii) and the moment of separation ($t = 0.587$ s, figure 2a iii), respectively. Figure 2(b) shows the gap $|d - D_p|/D_p$ between the two spheres as a function of time obtained from our simulation and those from the literature. It is seen that the simulated gap agrees with the literature within the limit of error, confirming the accuracy of the present PR-DNS code. Furthermore, since a short-range repulsive force model was employed in Breugem (2012) for calculating the collision force on spheres, we also perform the simulation by using the same repulsive force model (the solid black line). It shows that the simulated results agree well with Breugem (2012). It is worth noting that ACTM leads to a longer collision time, almost zero $|d - D_p|/D_p$ during the kissing process and a larger separation distance after contact as compared with the repulsive force model. These differences are not unexpected since the repulsive force model is only designed to prevent the particle overlapping with each other while ACTM for soft-sphere collision allows particle overlapping.

3. Simulation results

Figure 3 shows an instantaneous snapshot of two-phase flow after a statistically quasi-steady state is well established. The streamwise fluid velocity fluctuations $u'_f = u_f - \langle u_f \rangle$ are illustrated in several x - y and z - y slices, depicting high- and low-speed streaks typically observed in wall turbulence. The entrained particles jump between quasi-streamwise vortices and instantaneously locate in either low- or high-speed streaks. However, on average, particles preferentially accumulate in the low-speed streaks (not shown here). The illustration on the right of figure 3 presents the wall-normal profile of the mean solid indicator fraction $\langle \Phi \rangle$ defined by Kidanemariam et al. (2013), Kidanemariam & Uhlmann (2014) and Kidanemariam & Uhlmann (2017). Evidently, $\langle \Phi \rangle$ is roughly divided into two parts along the height. In the lower part, the profile of $\langle \Phi \rangle$ exhibits four bulges whose peak are 0.816, 0.794, 0.757 and 0.533, respectively. Note that the extreme value of the indicator fraction of densely packed particles on the stationary

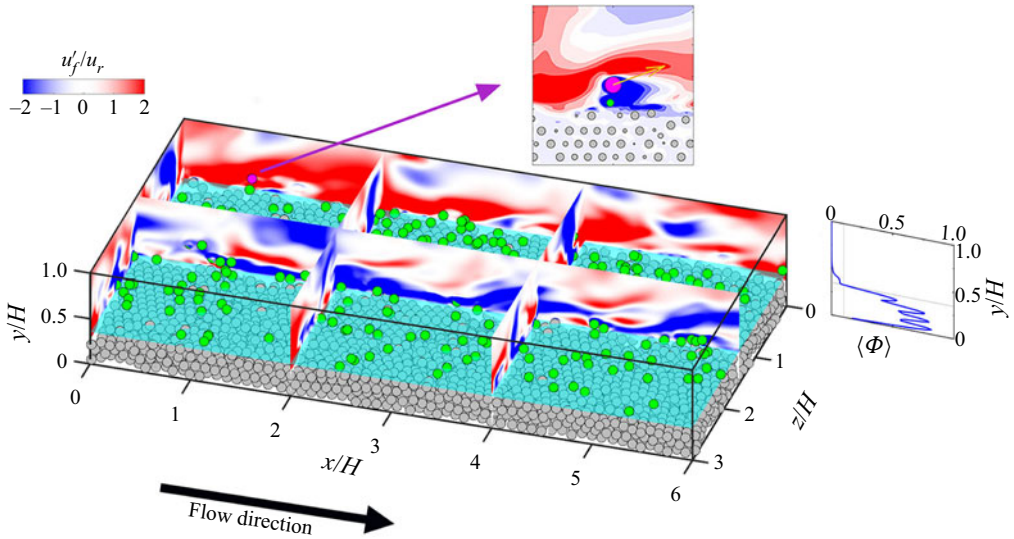


Figure 3. Instantaneous snapshot of particle distribution. Several slices depict the streamwise fluid velocity fluctuation u_f' . Particles above and below the mean interface height H_b are labelled in green and grey, respectively. The inset on the right shows the average indicator fraction profile $\langle \Phi \rangle$ of the solid particles. The top inset is the magnified view of the representative particle being tracked and its ambient flow at this moment.

bed surface should be 0.816 for hexagonal packing. In the upper part, however, a strong wall-normal particle concentration gradient forms due to the gravitational settling effect. The wall-normal location of the particle centres is overwhelming in the region of $y_p/H < 0.86$, where y_p is the vertical height of the centre of the particle. The rolling and saltating of the particles generate an uneven bed surface, indicating a significant erosion phenomenon. The averaged fluid–bed interface location H_b is extracted by means of a threshold value chosen as $\langle \Phi(y_p) \rangle = 0.1$ (Kidanemariam & Uhlmann 2014, 2017). In figure 3 the effective bed height of $H_b = 0.34$ is clearly shown by a cyan transparent plane, on which a mean interface shear stress τ_b is defined by the sum of the viscous stress, Reynolds stress and drag feedback (Kidanemariam & Uhlmann 2017). Therefore, the friction Reynolds number $Re_{\tau}^b = (H - H_b)u_{\tau}/\nu$ based on $H_f = H - H_b$ and the friction velocity u_{τ} defined as $= \sqrt{\tau_b/\rho_f}$ at H_b is equal to 91. Note that particles above and below the virtual interface are coloured green and grey, respectively.

At this moment, a representative ascending particle (the purple one) above H_b is selected for further Lagrangian tracing. The top inset of figure 3 is the magnified view of the representative particle being tracked and its ambient flow, in which the brown arrow marks out particle velocity. The smaller circles in the inset of figure 3 show the cross-section of surrounding particles on the x – z plane through the centre of the tracked sphere. It can be seen that the tracked particle locates in the high-speed region of incoming flow at this moment. However, the fluid velocity behind the particle is very low due to the complicated wake and particle–particle interaction.

3.1. The drag force along saltating particle trajectory

We show the time series of the dynamic responses of the tracked particle during two successive saltation processes in figure 4. The abscissa t is non-dimensionalized by the

Drag model of finite-sized particle in wall turbulence

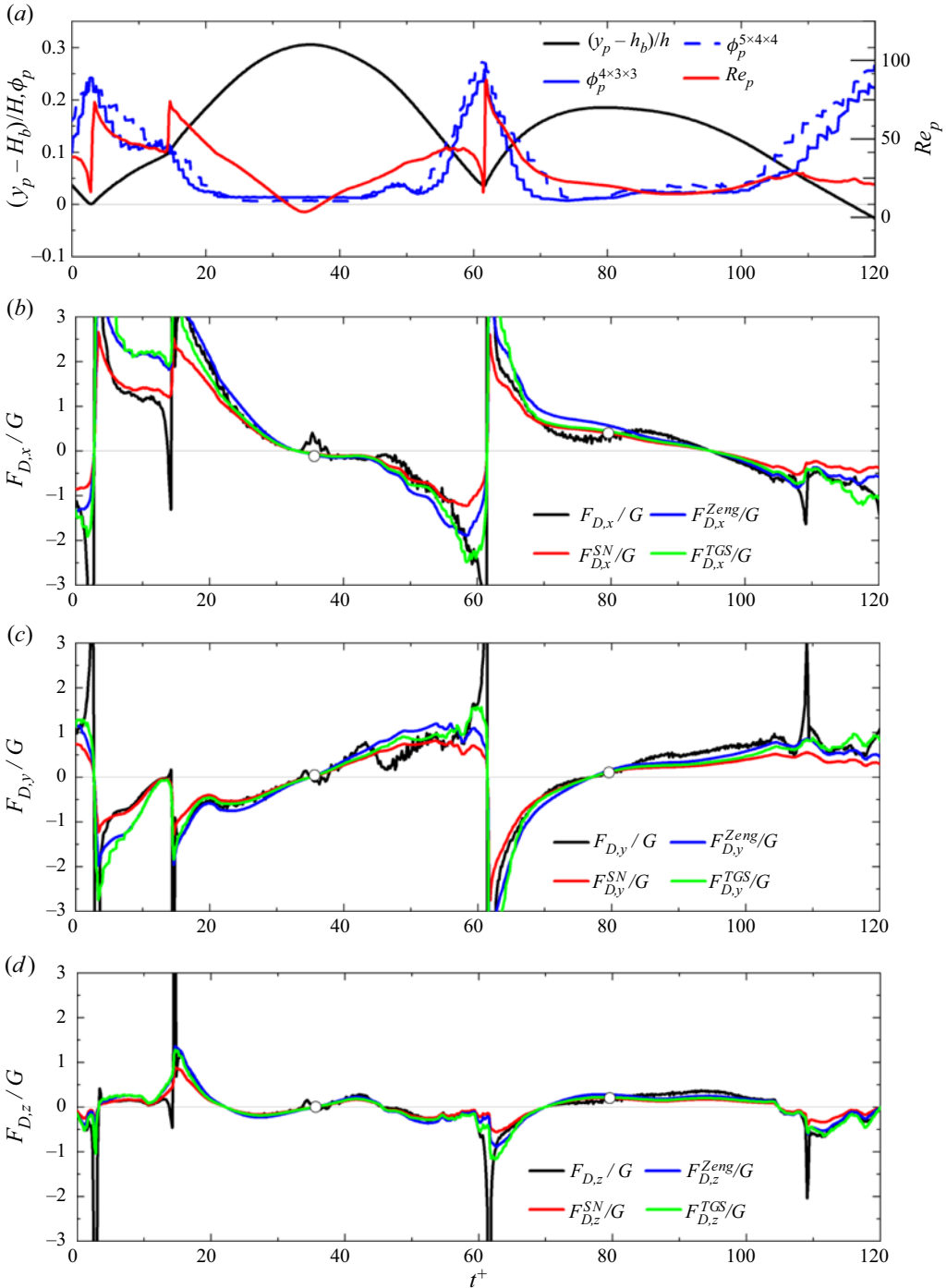


Figure 4. Dynamic responses of a typical saltating particle within two successive trajectories. (a) The height of the particle centre y_p , the local volume fraction around the tracked particle ϕ_p and the particle Reynolds number Re_p . (b) Time history of the streamwise component of the drag force. The solid black line is the PR-DNS results. The red, blue and green lines are the predicted results by models listed in table 1 respectively. (c,d) The same as (b), but for the wall-normal and spanwise components of the drag force.

inner scale of ν/u_τ^2 and starts from the moment, T_s , that the particle is tracked and, therefore, $t^+ = (T - T_s)u_\tau^2/\nu$. The time interval for the data output is $\Delta t^+ = 0.146$.

Figure 4(a) depicts the vertical height (the red line) of the particle centre y_p . It can be seen that the tracked particle reaches the vertexes of its parabolic-like trajectory at $t^+ = 32.26$ and $t^+ = 87.70$, and collides with other particles near the bed at $t^+ = 2.05$, $t^+ = 72.01$ and $t^+ = 114.10$. Note that the high and low trajectory vertexes are the direct results of different initial vertical take-off velocities for the two saltations. The local solid volume fraction ϕ_p (the blue line) and the particle Reynolds number Re_p (the black line) are presented in the meanwhile. The same method as Link *et al.* (2005) and Luo *et al.* (2021) is used to calculate ϕ_p , that is $\phi_p = \sum_{j \in \text{cell}} \alpha_{\text{cell}}^j V_{p,\text{cell}}^j / V_{\text{cell}}$, where $V_{p,\text{cell}}^j$ is the volume of a rectangular statistical cell around the particle, and α_{cell}^j is the ratio of the j th particle volume inside the statistical cell to the total particle volume. Here we use two different sizes of statistical cells to calculate ϕ_p . The unit size of $4D_p \times 3D_p \times 3D_p$ is denoted as $\phi_p^{4 \times 3 \times 3}$ and $5D_p \times 4D_p \times 4D_p$ is denoted as $\phi_p^{5 \times 4 \times 4}$. For a finite-sized particle, the particle Reynolds number Re_p cannot be defined unambiguously (Yu *et al.* 2017) since there are different definitions of slip velocity $\mathbf{u}_{slip} = \mathbf{u}_f^* - \mathbf{u}_p$ between the individual particle and the ambient turbulent flow. When an individual particle is fixed ($\mathbf{u}_p = 0$) in an unbounded domain, \mathbf{u}_{slip} can be simply taken to be the uniform inflow fluid velocity. In addition, the undisturbed flow velocity \mathbf{u}_f^* in previous studies can also be the flow velocity at the particle centre, the flow velocity averaged over the particle surface based on the Faxén's theorem, the flow velocity at a particle size in front of the particle and the flow velocity averaged over a spherical shell centred at the particle location with radius of R_s (Ganatos, Weinbaum & Pfeffer 1980a; Ganatos, Pfeffer & Weinbaum 1980b; Zeng *et al.* 2008; Cisse, Homann & Bec 2013; Akiki, Jackson & Balachandar 2017a; Akiki, Moore & Balachandar 2017b; Li *et al.* 2019; Luo *et al.* 2019, 2021), and so on. Zeng *et al.* (2008) argued that \mathbf{u}_f^* at the particle centre is adequate for the small particle in predicting the instantaneous force but, for larger particles, a weighted volume average flow velocity over a small sphere centred around the particle location is better. Then Kidanemariam *et al.* (2013) first proposed a method based on an average of the fluid velocity over a trimmed spherical surface around a particle. Li *et al.* (2019) also discussed the influence of different \mathbf{u}_f^* definitions on the prediction of the force acting on a particle with different diameters and placed within different regions of wall turbulence. The performance of different definitions of \mathbf{u}_f^* were revealed to be different. In the numerical simulation of a multiphase flow, it is especially difficult to determine the undisturbed fluid velocity seen by the particle since the flow has already been observably disturbed. We directly calculate \mathbf{u}_f^* in this study according to Cisse *et al.* (2013) and Luo *et al.* (2019, 2021) based upon the mass flux entering a spherical shell. To be specific, a spherical shell with a radius of $R_s = 3R_p$ is created by the Lagrangian grid generation scheme (Breugem 2012) and the fluid velocity can be easily interpolated to the Lagrangian grid by a trilinear interpolation method (Kidane-mariam *et al.* 2013; Chouippe & Uhlmann 2019). Then \mathbf{u}_{slip} is calculated according to the averaging method proposed by Cisse *et al.* (2013). The effects of R_s will be discussed in § 5, as well as other typical \mathbf{u}_f^* definitions.

It is seen from figure 4(a) that the local volume fraction around the particle ϕ_p varies in the same way as $\langle \Phi \rangle$ (above H_b) during its descending phase. Except for a visible plateau at approximately $8 < t^+ < 15$ where another particle enters and stays in the statistical cell of ϕ_p , there is no obvious qualitative difference between $\phi_p^{4 \times 3 \times 3}$ and $\phi_p^{5 \times 4 \times 4}$. Therefore, unless specifically stated in the following, the local volume fraction of particles ϕ_p is

always represented by $\phi_p^{4 \times 3 \times 3}$. On the contrary, the local volume fraction decreases rapidly during its ascending phase. One exception is the sudden weak bulge at approximately $t^+ = 50$, which should be attributed to the influence of bed particles since the tracked particle is now moving near the bed. The variation of the particle Reynolds number along its trajectory is a little bit complex however. Firstly, the smallest Re_p can be observed near (but not exactly at) the vertexes of particle trajectories. This is to be expected since particles are much easier to be accelerated by the flow away from the bed, resulting in relatively small slip velocities. Secondly, Re_p is very sensitive to the presence of the nearby particles. Taking the variation of Re_p within $8 < t^+ < 15$ as an example, the particle Reynolds number continuously decreases through the fluid-mediated particle–particle interaction, but suddenly increases when the other particles move away. And finally, an abrupt change in Re_p occurs before and after the collision, as shown during $t^+ = 0 \sim 5$ and $t^+ = 50 \sim 60$.

The solid black lines in figure 4(b–d) represent, respectively, the streamwise $F_{D,x}$, wall-normal ($F_{D,y}$) and spanwise ($F_{D,z}$) components of the drag force acting on the tracked particle along its trajectory from PR-DNS, normalized by the submerged weight $G = (\rho_p - \rho_f)gV_p$. Note that the circles in these figures mark out the vertexes of the particle trajectory. We address here that the drag force F_D is the projection of the hydrodynamic force on the direction of slip velocity, namely, $F_D = F_h \cos \alpha_F$, where α_F is the angle between the hydrodynamic force F_h and slip velocity u_{slip} . Several important features can be observed from the time history of the drag force. First, at each impact with the bed particles, the drag force peaks due to the collisions, which is consistent with that observed in Ji *et al.* (2014). Therefore, the maximum values of the y coordinate are just ± 3 in figure 4(b–d) to clearly show the drag force without collision. This sudden change is quickly damped by the hydrodynamic force. Second, there are sign changes of the drag force during both ascending and descending phases. However, the transition points of positive drag and negative drag force are not necessarily the same as the vertexes of the particle trajectory due to the complicated dynamics of turbulence–particle and particle–particle interactions. Third, the forces on the particle show substantial variations with time in addition to collision extremum during both ascending and descending phases; see, for example, $F_{D,z}$ during $21 < t^+ < 45$ and $F_{D,y}$ during $40 < t^+ < 55$. In previous studies on individual fixed particles (Zeng *et al.* 2008; Homann *et al.* 2013; Li *et al.* 2019) these features cannot be observed at the same time.

In figure 4(b–d) we also show the drag forces predicted by several typical drag models based on the same u_{slip} by DNS. The traditional drag models usually depend on 1 ~ 3 independent parameters to account for the different dynamics and parameter ranges. For the two-phase flow over the erodible bed concerned in this work, it is hard to distinguish the effects of the individual parameter. Since the mean/local shear, velocity fluctuation and the volume fraction all vary with wall-normal height in wall turbulence, we believe that the model that takes the particle-wall separation distance L into account is a good choice, in addition to the models that involve Re_p and ϕ_p . The statistics indicate that the particle Reynolds number in the simulation falls in the range of $0 < Re_p < 80$, and the solid volume fraction range is approximately $0 < \phi_p < 0.25$ for saltating particles. Therefore, the standard drag model (Schiller & Nauman 1935) of an isolated sphere that characterizes the Reynolds number dependence, the ϕ_p -dependent model proposed by Tenneti *et al.* (2011) and L -dependent model proposed by Zeng *et al.* (2009) are employed for comparison. Throughout the paper, these three models are denoted as SN, TGS and Zeng model for short and the predicted drag forces are F_D^{SN} , F_D^{TGS} and F_D^{Zeng} . The drag coefficient C_D of the three models are listed in table 1, according to which the drag force

Author & Year	Drag model	Parameter Range
Schiller & Nauman (1935)	$C_D^{SN} = \frac{24}{Re_p} (1 + 0.15 Re_p^{0.687})$	$Re_p < 800$
Zeng <i>et al.</i> (2009)	$C_D^{Zeng} = \frac{24}{Re_p} \left(1 + 0.138 \exp(-2L/H) + \frac{9}{16(1 + 2L/H)} \right) (1 + \alpha_D Re_p^{\beta_D})$ $\alpha_D = 0.15 - 0.046(1 - 0.16(L/H)^2) \exp(-0.7L/H)$ $\beta_D = 0.687 + 0.066(1 - 0.76(L/H)^2) \exp(-(L/H)^{0.9})$	$2 < Re_p < 250$
Tenneti <i>et al.</i> (2011)	$C_D^{TGS} = \frac{24(1 - \phi_p)}{Re_p} \left[\frac{C_D^{SN}(Re_p)}{(1 - \phi_p)^3} + \frac{5.81\phi_p}{(1 - \phi_p)^3} + \frac{0.48\phi_p^{1/3}}{(1 - \phi_p)^4} \right]$ $+ \phi_p^3 (1 - \phi_p) Re_p (0.95 + \frac{0.61\phi_p^3}{(1 - \phi_p)^3})$	$0.01 < Re_p < 300$ $0.1 < \phi_p < 0.5$

Table 1. Different drag force models. The predicted results from the SN, Zeng and TGS models, as shown in figure 4(b–d) and figure 8 as red, blue and green lines, respectively.

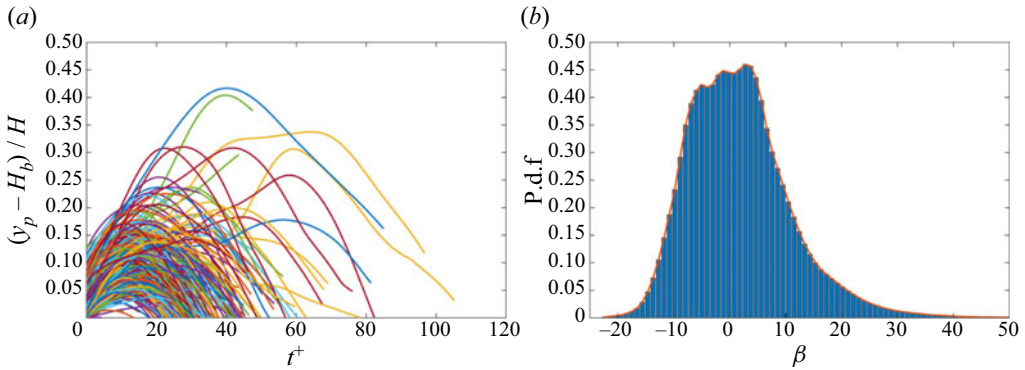


Figure 5. (a) All identified saltating trajectories shown by the vertical height versus saltation time. (b) The probability density distribution of the saltating angle.

can be given as $F_D = 1/8\pi\rho_f C_D D_p^2 |\mathbf{u}_{slip}| \mathbf{u}_{slip}$. From figure 4 we can see that even though the models qualitatively capture the trend of PR-DNS results, the quantitative differences remain clear.

Before quantitatively evaluating the drag models, we collect and pretreat the PR-DNS data according to several subjective criteria. The bed particles are first excluded since we place emphasis on particles that characterize the two-phase flow over the erodible bed. Then, particles that meet $H_{max,i} - H_{s,i} > 0.5D_p$ (Wiberg & Smith 1985) and $y_p - D_p/2 > H_b$ are identified as saltators, where $H_{max,i}$ and $H_{s,i}$ are the vertex of the i th saltating particle trajectory and particle initial take-off height, respectively. Note that the vertical position of the particle centre just finishes when the particle-bed collision is recorded as the initial take-off height of a saltating particle. From this moment (the initial take-off time, $t_{s,i}$) on, the i th particle moves in the fluid until falling back to the bed again at time $t_{e,i}$ due to gravity. All identified saltating trajectories are illustrated in figure 5(a) by their centre height, with regard to the inner-scale saltating time. Similar to Chouippe & Uhlmann (2019), we define the saltating angle between the particle vertical velocity $u_{p,y}$ and the horizontal plane as $\beta = \text{atan}(u_{p,y} / \sqrt{u_{p,x}^2 + u_{p,z}^2})$, which can also be used to describe the particle saltation. Apparently, $\beta > 0$ indicates the ascending phase, $\beta < 0$ indicates the descending phase and the particle reaches the vertex of its trajectory when $\beta = 0$. The probability density distribution of β is plotted in figure 5(b). It can be seen that, for the saltation particle trajectory on the erodible bed surface in this study, β is distributed between -20° and 40° .

The model-predicted drag forces are then assessed using scatter plots and the correlation R^2 values presented in figure 6, where R^2 is the statistical measure of how well the model prediction agrees with the actual PR-DNS data. By definition, a perfect model would have all the data points fall on the bisector, leading to $R^2 = 1$. With the decrease of R^2 to zero, the model predictions are completely irrelevant to PR-DNS results. For all frames, the abscissa and ordinate are for the PR-DNS and model-predicted results, respectively. Only streamwise and vertical components of the drag force are plotted in figure 6 since the spanwise component has similar comparison results as the streamwise component. In addition, the drag forces during descending and ascending phases are separately presented in consideration of the different dynamic responses shown in figure 4. Note that each point in the figure corresponds to the drag force on an individual particle at a given time,

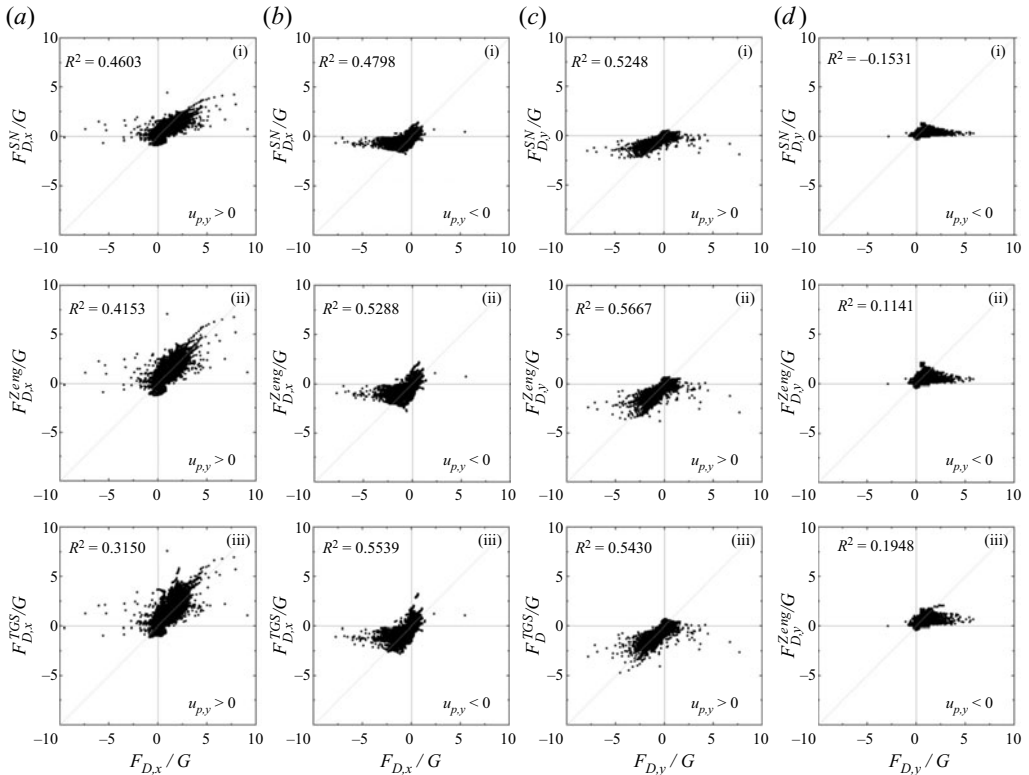


Figure 6. Detail comparisons between model-predicted and PR-DNS drag force (non-dimensionalized by the submerged weight) in streamwise and vertical direction during descending $u_{p,y} < 0$ and ascending $u_{p,y} > 0$ phases.

compared with the box-averaged pretreatment in several previous studies (Chen *et al.* 2020; Seyed-Ahmadi & Wachs 2020; Luo *et al.* 2021).

It can be seen from figure 6 that a number of scatters are in the second and fourth quadrants, which indicates that $\alpha_F > 90^\circ$. In this case, the drag models cannot be improved by simple C_D correction unless models are linearly superimposed with an additional contribution from the shear Reynolds number Re_γ (Lee & Balachandar 2010; Ekanayake *et al.* 2020, 2021) and nearby particles (Akiki *et al.* 2017*a,b*), and so on. The correlation R^2 between the predictions and PR-DNS results vary from case to case. In general, R^2 during the ascending phase is higher than the descending phase, partly because the particles have a large initial kinetic energy after collision with bed particles, which makes them less susceptible to turbulence and the nearby particles. While during the settling stage, particles accelerated by gravity ($F_{D,y}$ is applied almost in the opposite direction of motion) from zero $u_{p,y}$ are more prone to be influenced by neighbouring particles through the fluid-mediated interaction. The worst cases occur for $F_{D,y}$ during the descending phase, regardless of drag models. Here $R^2 < 0.2$ in $F_{D,y}$ frames indicates that PR-DNS results can hardly be predicted by the selected, typical drag models. We emphasize that the chaotic vortex shedding in the particle wake cannot be visibly observed at a relatively small particle Reynolds number (the maximum of Re_p is smaller than 80) in our simulation. In addition, it also shows that the volume fraction correction and particle-wall separation distance correction do improve the model predictions as compare to the classical SN

model. Therefore, it is necessary to establish a new drag model appropriate for the two-phase flow based on the above comparisons.

3.2. A new drag model for saltating particle in two-phase flow

Unlike widely used drag models for a particle stationary or translating parallel to a wall developed in wall flow, it might be more appropriate to establish the drag model along its trajectory for a saltating particle. We assume that the local drag force for an isolated sphere can be well predicted by the $C_D(Re_p)$ model, and the effect of other factors, the volume fraction, the particle-wall separation distance, turbulent velocity fluctuation and so on, are all integrated into a correction function C_R . Ideally, C_R involves only dimensionless particle velocity, at least in addition to Re_p , and with a simple form for applications. It is not unreasonable since the particle-wall separation distance and the local volume fraction experienced by particles depend strongly on the velocity of the particle, as shown in figures 3 and 4. Consequently, the related turbulent structures (depending on whether the particle is embedded within the viscous sublayer, buffer region or the log layer) and the fluid-mediated particle–particle interaction are implicitly involved. Before fitting the $C_R \propto u_{p,y}$ relation, we try to give a brief discussion.

As described in Appendix A, we assume that the ratio of the work $\int_{h_0}^{y_p} F_{h,y} \cdot dy$ done by the hydrodynamic force component $F_{h,y}$ to the potential energy $(1 - \rho_f/\rho_p)m_p(y_p - h_0)g$ is a constant according to the average energy and work plots (figure 12) and the initial position $h_0 = 0$, then we obtain the relationship for particle vertical velocity $u_{p,y}$ at height y_p , the initial vertical velocity $u_{p,0}$ and the vertex of a particle trajectory h_s in dimensionless form as

$$y_p^+ = h_s^+ \left(1 - u_{p,y}^2/u_{p,0}^2 \right). \quad (3.1)$$

If the particle is placed in the viscous sublayer of wall turbulence, then $y_p^+ = u_f^+$, and the slip velocity is $\mathbf{u}_{slip}^+ = \mathbf{u}_f^+ - \mathbf{u}_p^+ = [h_s^+(1 - u_{p,y}^2/u_{p,0}^2) - u_{p,x}^+]e_x - u_{p,y}^+e_y$. If the particle is placed in the log layer of wall turbulence and the mean fluid velocity satisfies $u_f^+ = (1/\kappa) \ln(y^+/y_0^+)$, where κ and y_0 are the von Kármán constant and the bed roughness, respectively, then the saltating height can be expressed as $y_p^+ = y_0^+(1 + \kappa u_f^+ + 1/2\kappa^2 u_f^{+2} + \dots)$. As a result, the slip velocity can be expressed as $\mathbf{u}_{slip}^+ = [h_s^+/\kappa y_0^+(1 - u_{p,y}^2/u_{p,0}^2) - 1/\kappa - u_{p,x}^+]e_x - u_{p,y}^+e_y$ by discarding higher-order terms. Nevertheless, such a rough discussion reveals that the slip velocity is approximately related to the n th power of the particle velocity. Let us assume that the relationship between u_{slip} and $u_{p,y}$ can approximately be $u_{slip} = f(u_{p,y}^n)$, with n ideally being approximately 2. Putting the relation into the Stokes formula, we get the expression of drag force as

$$F_D = kf(u_{p,y}^n), \quad (3.2)$$

where $k = 3\pi\rho_f D_p \nu$.

The standard drag curve of an isolated sphere characterizes Re_p dependence of the quasi-steady drag and is widely used as the benchmark mode for drag force corrections. We also use this scheme to develop the new drag force model. Figure 7(a) shows the ratio $|F_D|/|F_D^{SN}|$ of the PR-DNS drag forces to the drag forces predicted by the SN model as functions of Re_p and $u_{p,y}/u_{p,0}$. Again, the points of $|F_D|/|F_D^{SN}|$ are very scattered when Re_p or $u_{p,y}/u_{p,0}$ is fixed. It is hence unrealistic to directly pursue the

instantaneous drag force in a real turbulence laden with saltating particles. We therefore divide the data into different Re_p and $u_{p,y}/u_{p,0}$ bins. The widths of the bins are 2.5 and 0.25, respectively. Several typical $|F_D|/|F_D^{SN}| \propto Re_p$ and $|F_D|/|F_D^{SN}| \propto u_{p,y}/u_{p,0}$ curves are depicted in figure 7(b,c). It can be seen that $|F_D|/|F_D^{SN}|$ decreases with Re_p monotonously but changes with $u_{p,y}/u_{p,0}$ quadratically. Then we use the least square method to fit the data and get the fitting formula of the drag coefficient as

$$\left. \begin{aligned} C_D^{Fit} &= C_D^{SN} C_R, \\ C_R \left(Re_p, \frac{u_{p,y}}{u_{p,0}} \right) &= \frac{40 \left(\frac{u_{p,y}}{u_{p,0}} \right)^2 + 27}{Re_p} \end{aligned} \right\} \quad (3.3)$$

That is, the fitted drag coefficient is inversely proportional to Re_p and proportional to the particle speed squared. The fitted C_R is shown in figure 7(a) as a transparent surface. Note that the applicability of (3.3) is limited. On the one hand, the ranges of the used parameter are $0 < Re_p < 80$ and $-2.0 < u_{p,y}/u_{p,0} < 2.0$. Making further simulations for different values of D_p^+ and particle-to-fluid density ratios will extend the parameter range of the model. However, it is challenging because the Shields number will change as well, resulting in varying erodibility of the bed. On the other hand, sediment in the bed-load layer is actually transported via several modes: rolling/sliding and saltating. Saltation is the most dominant for the formation of a two-phase flow in the current case. According to the above data pretreatment and fitting process, we stress again that the proposed model is only applicable to saltating particles that have a parabola-like trajectory as shown in figure 5(a). In an Euler–Lagrange simulation of a two-phase flow formed by saltating particles, if the bed is not resolved, a splashing function is usually employed to determine the bed particle’s lift-off velocity and angle after a particle-bed collision (Zheng *et al.* 2021; Zhu *et al.* 2022). Therefore, the initial vertical velocity $u_{p,0}$ can be easily obtained. Then, the new model can be adopted for the trajectory simulation.

The mean drag forces \bar{F}_D along a particle trajectory predicted by the newly proposed model are plotted in figure 8, and compared against the PR-DNS results. Note that ‘along a particle trajectory’ here implies an average over the saltating angle β . The previous estimations that used particle-wall separation distance and volume fraction correction are also plotted in the same figure. The predictions from (3.3) agree well with the PR-DNS results, while the SN model underestimates the drag force on saltating particles the most even at the vertex of the trajectory where L - and ϕ_p -dependence are relatively low. We attribute this underestimation towards the nonlinear force-velocity relation. The turbulent velocity fluctuation will increase the mean drag force predicted by the SN model according to the analysis of Zeng *et al.* (2008). The TGS and Zeng models that involve, respectively, the correction of ϕ_p and L both improve the predictions to a certain extent. When $\beta > 10^\circ$, the Zeng model performs better than the TGS model, which means that the effect of local solid volume fraction is less significant near the bed during the ascending phase. While for $\beta < -10^\circ$, the TGS model predictions are more consistent with DNS. Note that very close to the bed, (3.3) predictions still deviate from DNS. This may be attributed to the deviation of saltating particle trajectory from the smooth parabola near the bed due to the presence of rolling particles. Consequently, the relationship between F_D and $u_{p,y}$ for $|u_{p,y}/u_{p,0}| > 1$ in figure 7(c) cannot be described by a quadratic function. This deviation can be eliminated to some degree by fitting the filtered data with $u_{p,y}/u_\tau$, see the orange dashed line,

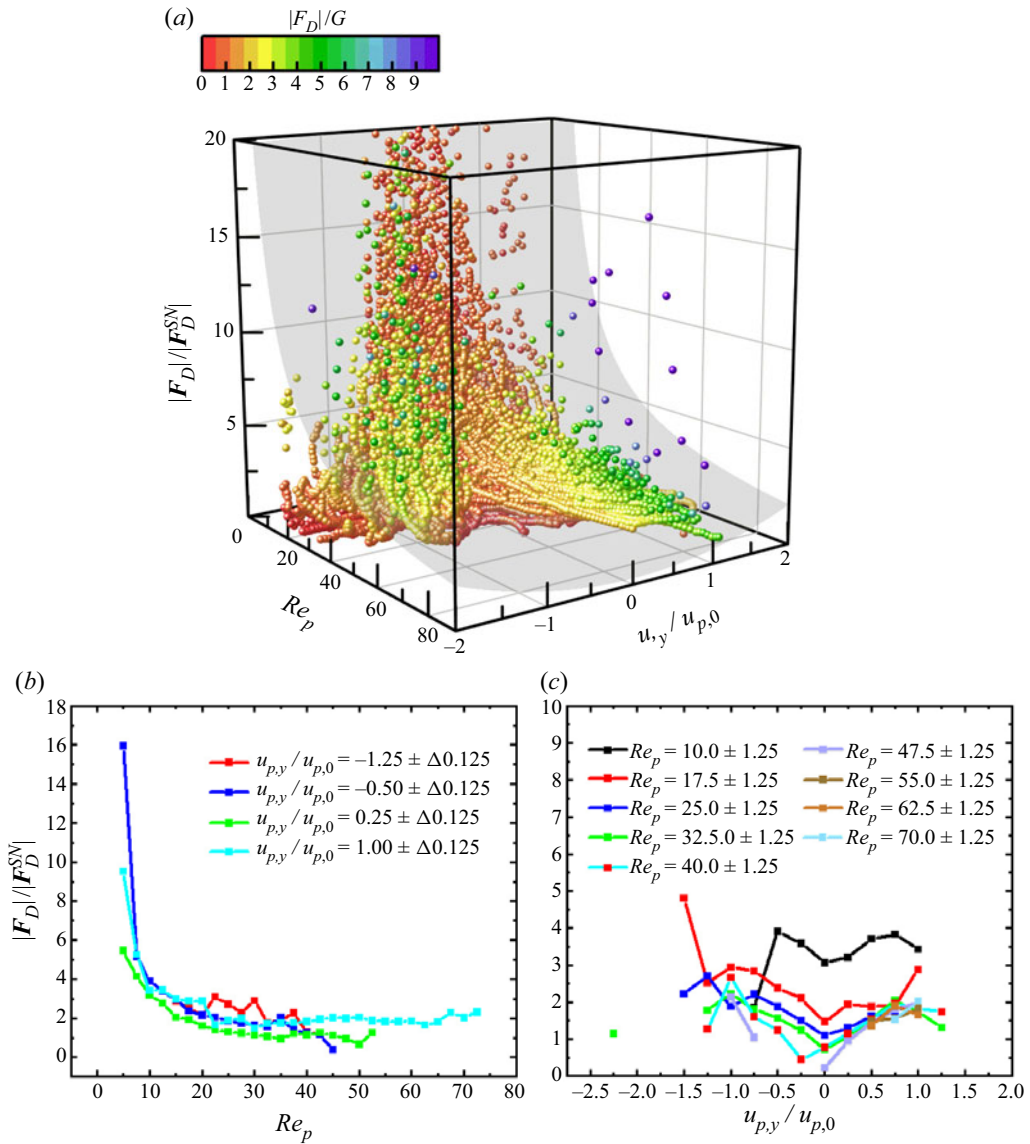


Figure 7. A comparison between the drag force obtained by PR-DNS and SN model as a function of Re_p with $u_{p,y}/u_{p,0}$.

though the underlying physics is not as clear as $u_{p,y}/u_{p,0}$ when describing a particle trajectory.

4. Discussion

As discussed in § 3, there are different definitions of the undisturbed flow velocity \mathbf{u}_f^* in previous studies. We calculate \mathbf{u}_{slip} according to Cisse *et al.* (2013) with a radius of $R_s = 3R_p$. However, the radius R_s of the spherical shell may affect \mathbf{u}_{slip} . We perform an additional elaboration with $R_s = 2R_p$ to evaluate the effects of R_s on the drag force. Figure 9(a) shows the DNS drag force along the trajectories of the same particle as in

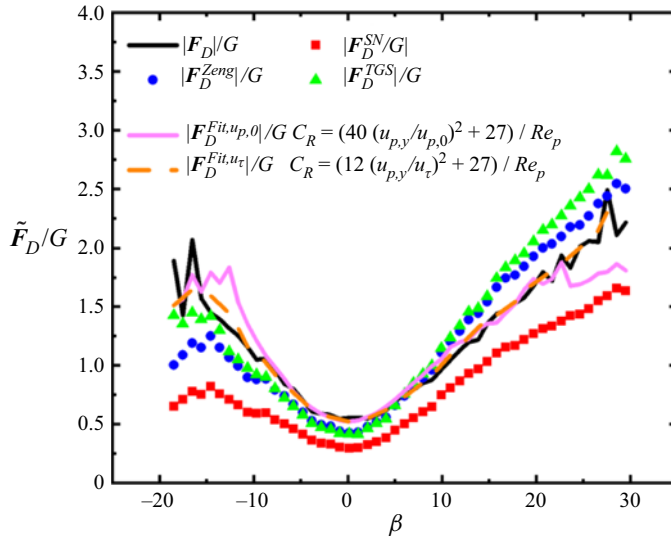


Figure 8. The mean drag force along particle trajectories in a two-phase flow over an erodible bed.

figure 4 with different R_s . In addition, we also calculate the slip velocity based on the undisturbed flow velocity averaged over the $R_s = 3R_p$ and $2R_p$ surface as Kidanemariam *et al.* (2013) and show the corresponding drag forces $F_D^{Kid,3R_p}$ and $F_D^{Kid,2R_p}$ in figure 9(a). Other methods for calculating the slip velocity, like the velocity at a point located one diameter in front of the particle and the undisturbed flow velocity at the particle centre from a companion DNS in the absence of particles, are either difficult to obtain or inappropriate. It is clear that the PR-DNS results are not very sensitive to R_s for both methods, as shown in figure 9(b). In the process of saltation, the drag forces obtained by the two methods are similar in the general trend, but quantitative differences remain especially when the particles take off from the bed after the collision. Here $F_D^{Kid,3R_p}$ and $F_D^{Kid,2R_p}$ drop rapidly to near zero and then increase to the level of F_D . Moreover, the fluctuation of drag force $\sigma_D^{Kid,3R_p}$ and $\sigma_D^{Kid,2R_p}$ seems to be smaller than σ_D when $\beta > 10^\circ$. Unfortunately, the underlying mechanics of the difference is not clear.

Let us move to the underlying dynamics of the drag force. It is clear that the forces on the particle are caused by the complicated dynamics of turbulence–particle and particle–particle interactions. Figure 10 shows snapshots of the fluid velocity fluctuation and vorticity around the particle at $t^+ = 44.00$, $t^+ = 46.93$ and $t^+ = 52.79$ to discern the influences. One can refer to figure 4 for the details along a particle trajectory. The brown, green and cyan arrows indicate the particle velocity, the slip velocity and hydrodynamic force, respectively. Within such a short time, the tracked particle is located in a somewhat high-speed streak, as shown in figure 10(a,c,e). Note that the low-speed wake behind the particle (the particle is large enough to create a wake behind it) interacts with turbulence, making it difficult to identify whether it is in a high-speed or low-speed streak. However, the streamwise component of the slip velocity is negative, indicating that the flow in front of the particle as it approaches the particle is high speed. At $t^+ = 44.00$, there is another nearby particle at the lower right of the tracked particle in figure 10(b). A positive local streamwise vorticity Ω_x region between the two particles is visible. This region becomes intense and elongates as the other particle comes closer at $t^+ = 46.93$ in figure 10(d). While at $t^+ = 52.79$, Ω_x shows an almost symmetrical, positive/negative vorticity region

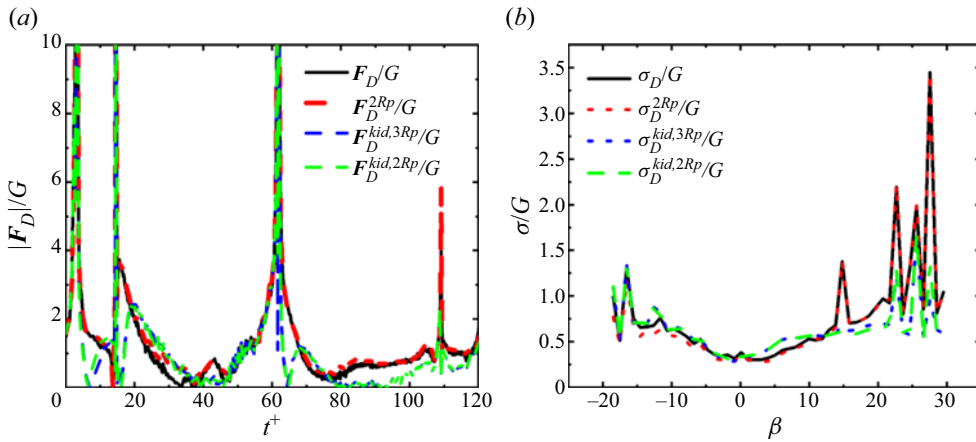


Figure 9. (a) Time histories of the drag force acting on the tracked particle in figure 4 based on different methods for calculating the slip velocity. (b) The fluctuating variances of the drag force along a particle trajectory.

near the upstream face of the particle in figure 10(f) when the nearby particle moves away. We emphasize that the approaching particle leads to a dramatic change in both hydrodynamic force and α_F in figure 10(b,d,f).

Obviously, the inclusion of the local volume fraction in the drag model cannot effectively improve the prediction of the drag force since the force on the particle related to the local volume fraction will be estimated to be the same as long as ϕ_p is the same within a given statistical box. This has already been confirmed by Akiki *et al.* (2017a) who further proposed a pairwise interaction extended point-particle model to account for the precise location of a few surrounding neighbours. The performance of this model was then validated by successfully simulating the sedimentation problems of 2, 5 and 80 sediment spheres with the DEM method. A pairwise interaction assumed that each adjacent disturbance flow is independent, then the effects of all neighbours are linearly superposed to obtain the total perturbation based on the pre-stored single neighbour, Re_p -dependent perturbation libraries. However, in a two-phase turbulent flow over the erodible bed, the single neighbour perturbation libraries also depend on the position of all neighbours themselves.

Finally, we address here that the drag force is defined as the hydrodynamic force in the direction of the slip velocity following Luo *et al.* (2021), which indicates that the unsteady effects are implicitly involved (at least partially) in the modified drag force. Similar treatment was also done by Bombardelli, Picano & Brandt (2016) who considered the drag coefficient C_D as a function of the Reynolds number and Strouhal number (the unsteady effect). In the traditional view (Maxey & Riley 1983), the hydrodynamic forces on an individual point particle can be written as the sum of the quasi-steady (the drag force), stress-gradient, added-mass and viscous-unsteady forces (the Basset force), etc. It is natural to wonder if the inclusion of the unsteady forces can improve the prediction since there are rapid changes in the force that are due to the rapid changes in particle motion (Zeng *et al.* 2008; Li *et al.* 2019). To this end, we subtract the fluid acceleration force F_{FA} , the added-mass force F_{AM} and the Basset history force F_{BA} from the total hydrodynamic force F_h to obtain the quasi-steady force F_{Steady} ($= F_h - F_{FA} - F_{AM} - F_{BA}$). According to the Maxey–Riley equation (Maxey & Riley 1983), F_{FA} , F_{AM} and F_{BA}

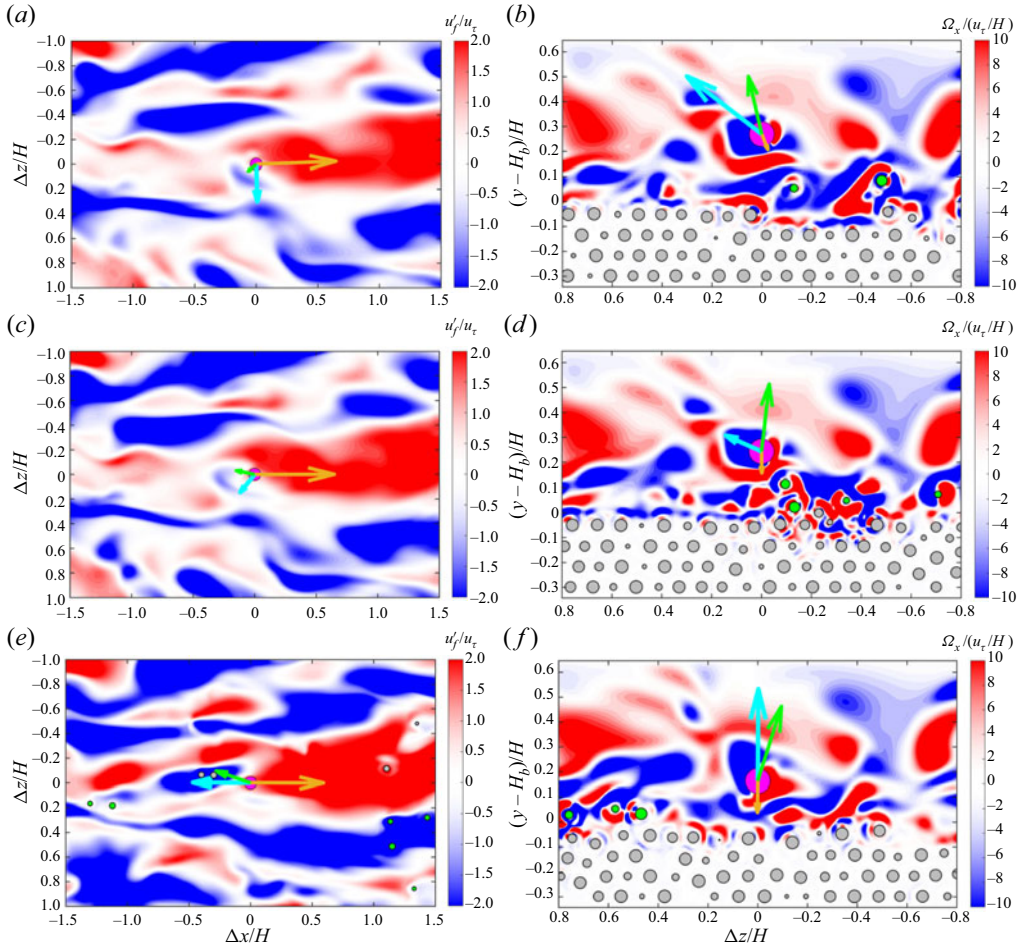


Figure 10. Snapshots of the streamwise fluid velocity fluctuation u'_f in the $x - z$ plane at (a) $t^+ = 44.00$, (b) $t^+ = 46.93$, (c) $t^+ = 52.79$. The spanwise vorticity Ω_x in the $z - y$ plane at the same time are presented in (b,d,f), respectively. The brown, green and cyan arrows indicate the particle velocity, the slip velocity and hydrodynamic force, respectively. The length of the arrows indicate the value of the variables.

on a solid particle can be expressed as

$$\left. \begin{aligned} \mathbf{F}_{FA} &= \rho_f \frac{m_p}{\rho_p} \frac{D\mathbf{u}_f}{Dt}, \\ \mathbf{F}_{AM} &= \frac{1}{2} \rho_f \frac{m_p}{\rho_p} \left(\frac{D\mathbf{u}_f}{Dt} - \frac{D\mathbf{u}_p}{Dt} \right), \\ \mathbf{F}_{BA} &= \frac{6\pi\mu(D_p/2)^2}{\sqrt{\pi\mu/\rho_f}} \left[\int_0^t K(t-\tau) \left(\frac{d\mathbf{u}_f}{dt} - \frac{d\mathbf{u}_p}{dt} \right) d\tau \right], \end{aligned} \right\} \quad (4.1)$$

The operator $D(\cdot)/Dt$ indicates the material derivative, K is the Basset kernel and τ is a dummy. Following Bombardelli, González & Niño (2015), a memory time period concept

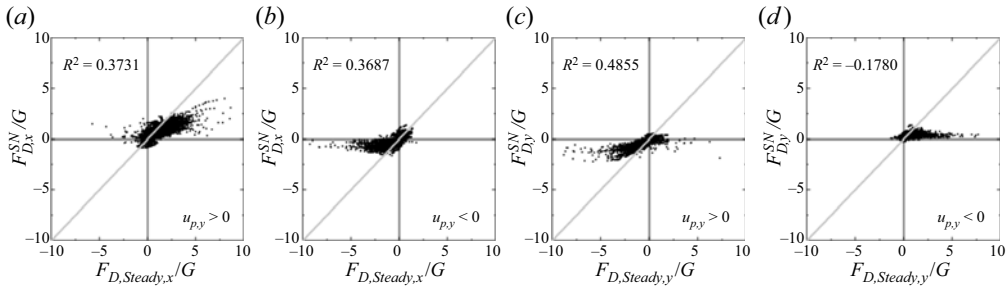


Figure 11. The comparisons between the SN-model-predicted drag force and the quasi-steady drag force during the descending $u_{p,y} < 0$ and ascending $u_{p,y} > 0$ phases.

is applied for the Basset kernel as

$$K(t - \tau) = \begin{cases} \frac{1}{\sqrt{t - \tau}}, & t - t_{window} < \tau < t, \\ 0, & \tau < t - t_{window}. \end{cases} \quad (4.2)$$

The projection of this quasi-steady hydrodynamic force component on the slip direction yields the quasi-steady drag force of $F_{D,Steady} = F_{Steady} \cos \alpha_F$. The detail comparisons between SN-model-predicted drag force and $F_{D,Steady}$ are presented in figure 11. Unfortunately, as compared with figure 6(a i–d i), R^2 is not fundamentally improved, which might be attributed to particle rotation taking place at anytime and anywhere along its trajectory.

5. Conclusions

In this study, particle saltation over the erodible bed in a turbulent open channel flow was numerically investigated using the DNS for turbulence flow, the fully resolved method and ACTM for particle dynamics and the IBM for the fluid–particle interaction. The drag force on saltating particles was presented along the particle trajectory. Typical drag models were employed to predict the drag force and compared against the PR-DNS results. According to the comparisons and the analysis on particle dynamics, a novel mean drag force model was proposed.

The particle volume fraction decreases rapidly along the height above the fluid–bed interface. Therefore, a saltating particle experiences a varying local volume fraction during its ascending and descending phases. Apart from inter-particle collision, the varying number of neighbouring particles, the turbulence structures around particles and the wake behind them make the drag force acting on particles in two-phase flow extremely complex. The typical SN model that characterizes the particle Reynolds number Re_p dependence, the TGS model that accounts for the joint influence of Re_p and local volume fraction ϕ_p , and the Zeng model that involves both Re_p and the particle-wall separation distance L , are employed to examine if these models are still accurate enough to predict the drag force on a particle in a turbulent flow over the erodible bed. It is found that these classical models originally developed for a single particle cannot predict accurately the drag force acting on saltating particles, especially during their descending phase.

Through simple theoretical analysis of particle velocity and slip velocity along a particle trajectory, we proposed that the drag force should be a function of particle vertical velocity to the n th power. Based on this consideration, we fitted the mean drag force along a particle

trajectory, taking the SN model as the benchmark model. The trajectory was described by the angle β between the particle vertical velocity and the horizontal plane. The corrected factor C_R for the drag force is inversely proportional to Re_p and proportional to the particle velocity (scaled by the initial take-off velocity $u_{p,0}$) squared. In addition, it is found that the performance of the new drag model can be further improved if the particle vertical velocity $u_{p,y}$ in the corrected factor is scaled by the friction velocity u_τ of the two-phase flow.

Due to the complicated combined influence of turbulence–particle and particle–particle interactions on particle dynamics, it is not possible so far to study the fluctuation of the drag force just based on $u_{p,y}$ and Re_p . Furthermore, the particle-to-fluid density ratio, the particle-to-fluid scale ratio, the Shield number and the turbulence Reynolds number will all play pivotal roles in the prediction of the drag force.

Acknowledgements. We thank the three anonymous referees for their useful comments.

Funding. X.J.Z. and Z.P.Z. are supported by the National Natural Science Foundation of China (grant number 92052202). P.W. and Y.H.N.L. are supported by the National Natural Science Foundation of China (grant number 12072138) and National Numerical Windtunnel project.

Declaration of interests. The authors report no conflict of interest.

Author ORCIDs.

① Ping Wang <https://orcid.org/0000-0001-7109-2473>;

② Yinghaonan Lei <https://orcid.org/0000-0003-0726-815X>;

③ Zhengping Zhu <https://orcid.org/0000-0002-1315-3554>;

④ Xiaojing Zheng <https://orcid.org/0000-0002-6845-2949>.

Appendix A

The motion equation of particles (without collision force) in the vertical direction is

$$m_p \frac{du_{p,y}}{dt} = V_p(\rho_p - \rho_f)g + F_{h,y}, \quad (\text{A1})$$

where V_p and $F_{h,y}$ are the volume of the spheroidal particle and the vertical component of the hydrodynamic force. The works done by each term after distance $dy = u_{p,y} dt$ are

$$m_p \frac{du_{p,y}}{dt} \cdot u_{p,y} dt = V_p(\rho_p - \rho_f)g \cdot dy + F_{h,y} \cdot dy. \quad (\text{A2})$$

By integrating the above equation from 0 to t (from h_0 to y_p),

$$\int_0^t m_p \frac{du_{p,y}}{dt} \cdot u_{p,y} dt = \int_{h_0}^{y_p} V_p(\rho_p - \rho_f)g \cdot dy + \int_{h_0}^{y_p} F_{h,y} \cdot dy, \quad (\text{A3})$$

we can get

$$m_p \left(\frac{u_{p,y}^2}{2} - \frac{u_{p,0}^2}{2} \right) = V_p(\rho_p - \rho_f)g \cdot (y_p - h_0) + \int_{h_0}^{y_p} F_{h,y} \cdot dy \quad (\text{A4})$$

or

$$m_p \left(\frac{u_{p,y}^2}{2} - \frac{u_{p,0}^2}{2} \right) = (1 - \rho_f/\rho_p)m_p(y_p - h_0)g + \int_{h_0}^{y_p} F_{h,y} \cdot dy. \quad (\text{A5})$$

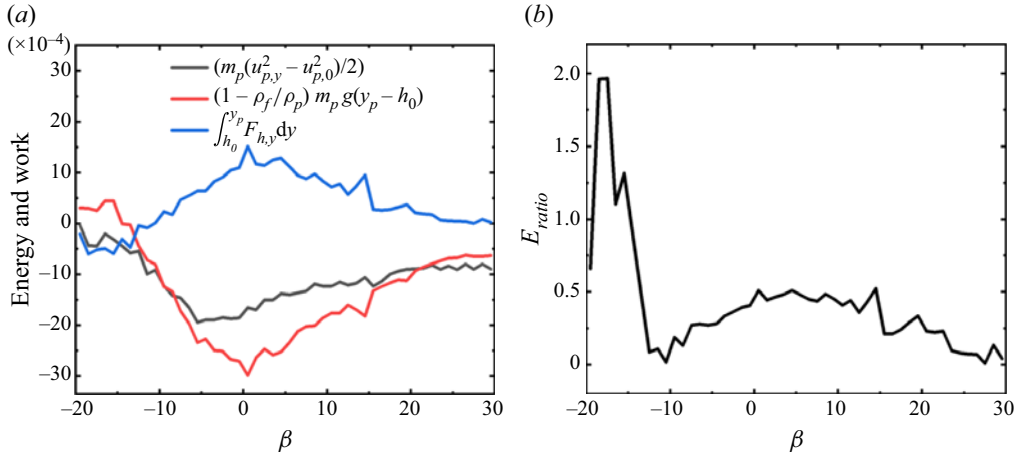


Figure 12. (a) The kinetic energy, potential energy and work done by the vertical component of the hydrodynamic force along a particle trajectory, averaged over β . (b) Ratio of the work done by the vertical component of the hydrodynamic force to potential energy.

At the vertex h_s of a particle trajectory, we have

$$-\frac{1}{2}m_p u_{p,0}^2 = (1 - \rho_f/\rho_p)m_p(h_s - h_0)g + \int_{h_0}^{h_s} F_{h,y} \cdot dy. \quad (A6)$$

Dividing (A5) by (A6) yields

$$1 - \frac{u_{p,y}^2}{u_{p,0}^2} = \frac{(1 - \rho_f/\rho_p)m_p(y_p - h_0)g + \int_{h_0}^{y_p} F_{h,y} \cdot dy}{(1 - \rho_f/\rho_p)m_p(h_s - h_0)g + \int_{h_0}^{h_s} F_{h,y} \cdot dy}. \quad (A7)$$

The kinetic energy, potential energy and the work done by the hydrodynamic force component $F_{h,y}$ along a particle trajectory are plotted in figure 12. It is found that the ratio E_{ratio} of $\int_{h_0}^{y_p} F_{h,y} \cdot dy$ to $(1 - \rho_f/\rho_p)m_p(y_p - h_0)g$ is approximately 0.0–0.5 except for $\beta < -12^\circ$ (particles settle near the bed surface) and $\beta > 25^\circ$ (where the probability density distribution of β is low). Although the ratio varies with β , let us assume that the ratio E_{ratio} is equal to a constant value B and the right-hand side of (A7) becomes

$$\frac{(1 - \rho_f/\rho_p)m_p(y_p - h_0)g + B(y_p - h_0)}{(1 - \rho_f/\rho_p)m_p(h_s - h_0)g + B(h_s - h_0)}. \quad (A8)$$

Then, the simple theoretical analysis and assumption yield

$$\frac{u_{p,y}^2}{u_{p,0}^2} \approx \frac{h_s - y_p}{h_s - h_0}. \quad (A9)$$

REFERENCES

- AKIKI, G., JACKSON, T.L. & BALACHANDAR, S. 2017a Pairwise interaction extended point-particle model for a random array of monodisperse spheres. *J. Fluid Mech.* **813**, 882–928.
 AKIKI, G., MOORE, W.C. & BALACHANDAR, S. 2017b Pairwise-interaction extended point-particle model for particle-laden flows. *J. Comput. Phys.* **351**, 329–357.

- ANCEY, C., DAVISON, A.C., BÖHM, T., JODEAU, M. & FREY, P. 2008 Entrainment and motion of coarse particles in a shallow water stream down a steep slope. *J. Fluid Mech.* **595**, 83–114.
- APTE, S.V., MARTIN, M. & PATANKAR, N.A. 2009 A numerical method for fully resolved simulation (FRS) of rigid particle-flow interactions in complex flows. *J. Comput. Phys.* **228**, 2712–2738.
- ARDEKANI, M.N., AL ASMAR, L., PICANO, F. & BRANDT, L. 2018 Numerical study of heat transfer in laminar and turbulent pipe flow with finite-size spherical particles. *Intl J. Heat Fluid Flow* **71**, 189–199.
- AYYALASOMAYAJULA, S., GYLFASON, A., COLLINS, L.R., BODENSCHATZ, E. & WARHAFT, Z. 2006 Lagrangian measurements of inertial particle accelerations in grid generated wind tunnel turbulence. *Phys. Rev. Lett.* **97** (14), 144507.
- BALACHANDAR, S. & EATON, J.K. 2010 Turbulent dispersed multiphase flow. *Annu. Rev. Fluid Mech.* **42** (1), 111–133.
- BATCHELOR, G.K. 1972 Sedimentation in a dilute dispersion of spheres. *J. Fluid Mech.* **52** (2), 245–268.
- BEETSTRA, R., VAN DER HOEF, M.A. & KUIPERS, J.A.M. 2007 Drag force of intermediate Reynolds number flow past mono- and bidisperse arrays of spheres. *AIChE J.* **53** (2), 489–501.
- BERZI, D., JENKINS, J.T. & VALANCE, A. 2016 Periodic saltation over hydrodynamically rough beds: aeolian to aquatic. *J. Fluid Mech.* **786**, 190–209.
- BIEGERT, E., VOWINCKEL, B. & MEIBURG, E. 2017 A collision model for grain-resolving simulations of flows over dense, mobile, polydisperse granular sediment beds. *J. Comput. Phys.* **340**, 105–127.
- BOMBARDELLI, F.A., GONZÁLEZ, A.E. & NIÑO, Y.I. 2015 Computation of the particle basset force with a fractional-derivative approach. *ASCE J. Hydraul. Engng* **134** (10), 1513–1520.
- BOMBARDELLI, W., PICANO, F. & BRANDT, L. 2016 Sedimentation of finite-size spheres in quiescent and turbulent environments. *J. Fluid Mech.* **788** (669), 650–669.
- BRANDT, L. & COLETTI, F. 2022 Particle-laden turbulence: progress and perspectives. *Annu. Rev. Fluid Mech.* **54** (1), 159–189.
- BREUGEM, W.P. 2012 A second-order accurate immersed boundary method for fully resolved simulations of particle-laden flows. *J. Comput. Phys.* **231** (13), 4469–4498.
- CAO, C., CHEN, S., LI, J., LIU, Z., ZHA, L., BAO, S. & ZHENG, C. 2015 Simulating the interactions of two freely settling spherical particles in Newtonian fluid using lattice-Boltzmann method. *Appl. Maths Comput.* **250**, 533–551.
- CAPELATRO, J. & DESJARDINS, O. 2013 An Euler–Lagrange strategy for simulating particle-laden flows. *J. Comput. Phys.* **238**, 1–31.
- CATE, A.T., DERKSEN, J.J., PORTELA, L.M. & AKKER, H.E.A.V.D. 2004 Fully resolved simulations of colliding monodisperse spheres in forced isotropic turbulence. *J. Fluid Mech.* **519**, 233–271.
- CHEN, X., SONG, N., JIANG, M., MA, T. & ZHOU, Q. 2020 A microscopic gas–solid drag model considering the effect of interface between dilute and dense phases. *Intl J. Multiphase Flow* **128**, 103266.
- CHOUPIPE, A. & UHLMANN, M. 2019 On the influence of forced homogeneous-isotropic turbulence on the settling and clustering of finite-size particles. *Acta Mech.* **230** (2), 387–412.
- CISSE, M., HOMANN, H. & BEC, J. 2013 Slipping motion of large neutrally buoyant particles in turbulence. *J. Fluid Mech.* **735**, R1.
- COSTA, P., BOERSMA, B.J., WESTERWEEEL, J. & BREUGEM, W.P. 2015 Collision model for fully resolved simulations of flows laden with finite-size particles. *Phys. Rev. E* **92** (5), 053012.
- COSTA, P., BRANDT, L. & PICANO, F. 2020 Interface-resolved simulations of small inertial particles in turbulent channel flow. *J. Fluid Mech.* **883**, A54.
- DARMANA, D., DEEN, N.G. & KUIPERS, J.A.M. 2006 Parallelization of an Euler–Lagrange model using mixed domain decomposition and a mirror domain technique: application to dispersed gas–liquid two-phase flow. *J. Comput. Phys.* **220** (1), 216–248.
- DEEN, N.G., VAN SINT ANNALAND, M., VAN DER HOEF, M.A. & KUIPERS, J.A.M. 2007 Review of discrete particle modeling of fluidized beds. *Chem. Engng Sci.* **62** (1), 28–44.
- DRITSELIS, C.D. & VLACHOS, N.S. 2008 Numerical study of educed coherent structures in the near-wall region of a particle-laden channel flow. *Phys. Fluids* **20** (5), 055103.
- EATON, J.K. 2009 Two-way coupled turbulence simulations of gas-particle flows using point-particle tracking. *Intl J. Multiphase Flow* **35** (9), 792–800.
- EKANAYAKE, N.I.K., BERRY, J.D. & HARVIE, D.J.E. 2021 Lift and drag forces acting on a particle moving in the presence of slip and shear near a wall. *J. Fluid Mech.* **915**, A103.
- EKANAYAKE, N.I.K., BERRY, J.D., STICKLAND, A.D., DUNSTAN, D.E., MUIR, I.L., DOWER, S.K. & HARVIE, D.J.E. 2020 Lift and drag forces acting on a particle moving with zero slip in a linear shear flow near a wall. *J. Fluid Mech.* **904**, A6.
- EPSTEIN, N. 1954 Viscous flow in multiparticle systems: Cubical assemblages of uniform spheres. PhD thesis, New York University.

- ERGUN, S. 1952 Fluid flow through packed columns. *J. Mater. Sci. Chem. Engng* **48** (2), 89–94.
- ESMAILY, M. & HORWITZ, J.A.K. 2018 A correction scheme for two-way coupled point-particle simulations on anisotropic grids. *J. Comput. Phys.* **375**, 960–982.
- ESTEGHAMATI, A., EUZENAT, F., HAMMOUTI, A., LANCE, M. & WACHS, A. 2018 A stochastic formulation for the drag force based on multiscale numerical simulation of fluidized beds. *Intl J. Multiphase Flow* **99**, 363–382.
- FAND, R.M., KIM, B.Y.K., LAM, A.C.C. & PHAN, R.T. 1987 Resistance to the flow of fluids through simple and complex porous media whose matrices are composed of randomly packed spheres. *Trans. ASME J. Fluids Engng* **109** (3), 268–273.
- FAXÉN, H. 1922 Der Widerstand gegen die Bewegung einer starren Kugel in einer zähen Flüssigkeit, die zwischen zwei parallelen ebenen Wänden eingeschlossen ist. *Ann. Phys.* **373** (10), 89–119.
- FENG, J., HU, H.H. & JOSEPH, D.D. 1994a Direct simulation of initial value problems for the motion of solid bodies in a newtonian fluid. Part 1. Sedimentation. *J. Fluid Mech.* **261**, 95–134.
- FENG, J., HU, H.H. & JOSEPH, D.D. 1994b Direct simulation of initial value problems for the motion of solid bodies in a Newtonian fluid. Part 2. Couette and Poiseuille flows. *J. Fluid Mech.* **277**, 271–301.
- FORNARI, W., ZADE, S., BRANDT, L. & PICANO, F. 2019 Settling of finite-size particles in turbulence at different volume fractions. *Acta Mech.* **230** (2), 413–430.
- FORTES, A.F., JOSEPH, D.D. & LUNDGREN, T.S. 1987 Nonlinear mechanics of fluidization of beds of spherical particles. *J. Fluid Mech.* **177**, 467–483.
- GANATOS, P., PFEFFER, R. & WEINBAUM, S. 1980b A strong interaction theory for the creeping motion of a sphere between plane parallel boundaries. Part 2. Parallel motion. *J. Fluid Mech.* **99** (4), 755–783.
- GANATOS, P., WEINBAUM, S. & PFEFFER, R. 1980a A strong interaction theory for the creeping motion of a sphere between plane parallel boundaries. Part 1. Perpendicular motion. *J. Fluid Mech.* **99** (4), 739–753.
- GAO, H., LI, H. & WANG, L.P. 2013 Lattice Boltzmann simulation of turbulent flow laden with finite-size particles. *Comput. Maths Applics.* **65** (2), 194–210.
- GLOWINSKI, R., PAN, T.W., HESLA, T.I., JOSEPH, D.D. & PERIAUX, J. 2001 A fictitious domain approach to the direct numerical simulation of incompressible viscous flow past moving rigid bodies: application to particulate flow. *J. Comput. Phys.* **169** (2), 363–426.
- GRBAVIC, Z.B., GARIC, R.V., HADZISMAJLOVIC, D.E., JOVANOVIĆ, S., VUKOVIĆ, D.V., LITTMAN, H. & MORGAN, M.H. 1991 Variational model for prediction of the fluid-particle interphase drag coefficient and particulate expansion of fluidized and sedimenting beds. *Powder Technol.* **68** (3), 199–211.
- GUAN, L.H., SALINAS, J., ZGHEIB, N. & BALACHANDAR, S. 2021 Force and torque model sensitivity and coarse graining for bedload-dominated sediment transport. *Eur. J. Mech. B/Fluids* **90**, 137–151.
- HAPPEL, J. & BRENNER, H. 1981 *Low Reynolds Number Hydrodynamics*. Springer Science & Business Media.
- HASIMOTO, H. 1959 On the periodic fundamental solutions of the Stokes equations and their application to viscous flow past a cubic array of spheres. *J. Fluid Mech.* **5** (2), 317–328.
- HOMANN, H., BEC, J. & GRAUER, R. 2013 Effect of turbulent fluctuations on the drag and lift forces on a towed sphere and its boundary layer. *J. Fluid Mech.* **721**, 155–179.
- HU, H.H., PATANKAR, N.A. & ZHU, M.Y. 2001 Direct numerical simulations of fluid–solid systems using the arbitrary Lagrangian–Eulerian technique. *J. Comput. Phys.* **169** (2), 427–462.
- HUANG, Z.Q., WANG, H.Z., ZHOU, Q. & LI, T.W. 2017 Effects of granular temperature on inter-phase drag in gas–solid flows. *Powder Technol.* **321**, 435–443.
- JI, C., MUNJIZA, A., AVITAL, E., MA, J. & WILLIAMS, J.J.R. 2013 Direct numerical simulation of sediment entrainment in turbulent channel flow. *Phys. Fluids* **25** (5), 056601.
- JI, C.N., MUNJIZA, A., AVITAL, E., XU, D. & WILLIAMS, J. 2014 Saltation of particles in turbulent channel flow. *Phys. Rev. E* **89** (5), 052202.
- JIN, T., WANG, P. & ZHENG, X.J. 2021 Characterization of wind-blown sand with near-wall motions and turbulence: from grain-scale distributions to sediment transport. *J. Geophys. Res.* **126**, e2021JF006234.
- KEMPE, T. & FRÖHLICH, J. 2012 Collision modelling for the interface-resolved simulation of spherical particles in viscous fluids. *J. Fluid Mech.* **709**, 445–489.
- KIDANEMARIAM, A.G., CHAN-BRAUN, C., DOYCHEV, T. & UHLMANN, M. 2013 Direct numerical simulation of horizontal open channel flow with finite-size, heavy particles at low solid volume fraction. *New J. Phys.* **15** (2), 025031.
- KIDANEMARIAM, A.G. & UHLMANN, M. 2014 Interface-resolved direct numerical simulation of the erosion of a sediment bed sheared by laminar channel flow. *Intl J. Multiphase Flow* **67**, 174–188.
- KIDANEMARIAM, A.G. & UHLMANN, M. 2017 Formation of sediment patterns in channel flow: minimal unstable systems and their temporal evolution. *J. Fluid Mech.* **818**, 716–743.
- KIM, J. & MOIN, P. 1985 Application of a fractional-step method to incompressible Navier–Stokes equations. *J. Comput. Phys.* **59** (2), 308–323.

- LASHGARI, I., PICANO, F., BREUGEM, W.P. & BRANDT, L. 2016 Channel flow of rigid sphere suspensions: particle dynamics in the inertial regime. *Intl J. Multiphase Flow* **78**, 12–24.
- LASHGARI, I., PICANO, F., COSTA, P., BREUGEM, W.P. & BRANDT, L. 2017 Turbulent channel flow of a dense binary mixture of rigid particles. *J. Fluid Mech.* **818**, 623–645.
- LEE, H. & BALACHANDAR, S. 2010 Drag and lift forces on a spherical particle moving on a wall in a shear flow at finite *Re*. *J. Fluid Mech.* **657**, 89–125.
- LI, X., BALACHANDAR, S., LEE, H. & BAI, B.F. 2019 Fully resolved simulations of a stationary finite-sized particle in wall turbulence over a rough bed. *Phys. Rev. Fluids* **4** (9), 094302.
- LI, R.Y., HUANG, W.X., ZHAO, L.H. & XU, C.X. 2020 Assessment of force models on finite-sized particles at finite Reynolds numbers. *Appl. Math. Mech.* **41** (6), 953–966.
- LI, Y.M., MCLAUGHLIN, J.B., KONTOMARIS, K. & PORTELA, L. 2001 Numerical simulation of particle-laden turbulent channel flow. *Phys. Fluids* **13** (10), 2957–2967.
- LIAO, C.C., HSIAO, W.W., LIN, T.Y. & LIN, C.A. 2015 Simulations of two sedimenting-interacting spheres with different sizes and initial configurations using immersed boundary method. *Comput. Mech.* **55** (6), 1191–1200.
- LINK, J.M., CUYPERS, L.A., DEEN, N.G. & KUIPERS, J.A.M. 2005 Flow regimes in a spout–fluid bed: a combined experimental and simulation study. *Chem. Engng Sci.* **60** (13), 3425–3442.
- LUCCI, F., FERRANTE, A. & ELGHOBASHI, S. 2010 Modulation of isotropic turbulence by particles of Taylor length-scale size. *J. Fluid Mech.* **650**, 5–55.
- LUCCI, F., FERRANTE, A. & ELGHOBASHI, S. 2011 Is Stokes number an appropriate indicator for turbulence modulation by particles of Taylor-length-scale size? *Phys. Fluids* **23** (2), 025101.
- LUO, K., TAN, J.H., WANG, Z.L. & FAN, J.R. 2016 Particle-resolved direct numerical simulation of gas–solid dynamics in experimental fluidized beds. *AIChE J.* **62** (6), 1917–1932.
- LUO, K., WANG, D., JIN, T., WANG, S., WANG, Z., TAN, J.H. & FAN, J.R. 2021 Analysis and development of novel data-driven drag models based on direct numerical simulations of fluidized beds. *Chem. Engng Sci.* **231**, 116245.
- LUO, K., WANG, Z., TAN, J.H. & FAN, J.R. 2019 An improved direct-forcing immersed boundary method with inward retraction of Lagrangian points for simulation of particle-laden flows. *J. Comput. Phys.* **376**, 210–227.
- MAXEY, M.R. & RILEY, J.J. 1983 Equation of motion for a small rigid sphere in a nonuniform flow. *Phys. Fluids* **26** (4), 883.
- NASO, A. & PROSPERETTI, A. 2010 The interaction between a solid particle and a turbulent flow. *New J. Phys.* **12** (3), 033040.
- OSEEN, C.W. 1910 Über die Stokes' sche Formel und über eine verwandte Aufgabe in der Hydrodynamik. *Ark. Mat. Astron. Fys.* **6**, 1.
- PÄHTZ, T., CLARK, A.H., VALYRAKIS, M. & DURÁN, O. 2020 The physics of sediment transport initiation, cessation, and entrainment across aeolian and fluvial environments. *Rev. Geophys.* **58** (1), e2019RG000679.
- PÄHTZ, T., VALYRAKIS, M., ZHAO, X.H. & LI, Z.S. 2018 The critical role of the boundary layer thickness for the initiation of aeolian sediment transport. *Geosciences* **8** (9), 314.
- PAN, Y. & BANERJEE, S. 1997 Numerical investigation of the effects of large particles on wall-turbulence. *Phys. Fluids* **9** (12), 3786–3807.
- PESKIN, C.S. 1977 Numerical analysis of blood flow in the heart. *J. Comput. Phys.* **25** (3), 220–252.
- PROUDMAN, I. & PEARSON, J.R.A. 1957 Expansions at small Reynolds numbers for the flow past a sphere and a circular cylinder. *J. Fluid Mech.* **2** (3), 237–262.
- QURESHI, N.M., ARRIETA, U., BAUDET, C., CARTELLIER, A., GAGNE, Y. & BOURGOIN, M. 2008 Acceleration statistics of inertial particles in turbulent flow. *Eur. Phys. J. B* **66** (4), 531–536.
- ROUSON, D.W.I. 1997 *A Direct Numerical Simulation of a Particle-Laden Turbulent Channel Flow*. Stanford University.
- ROUSON, D.W.I. & EATON, J.K. 2001 On the preferential concentration of solid particles in turbulent channel flow. *J. Fluid Mech.* **428**, 149–169.
- RUMPF, H.C.H. & GUPTE, A.R. 1971 Einflüsse der Porosität und Korngrößenverteilung im Widerstandsgesetz der Porenströmung. *Chem. Ing. Tech.* **43** (6), 367–375.
- SANGANI, A.S. & ACRIVOS, A. 1982 Slow flow through a periodic array of spheres. *Intl J. Multiphase Flow* **8** (4), 343–360.
- SCHANZ, D., GESEMANN, S. & SCHRÖDER, A. 2016 Shake-the-box: Lagrangian particle tracking at high particle image densities. *Exp. Fluids* **57** (5), 70.
- SCHILLER, L. & NAUMAN, A. 1935 A drag coefficient correlation. *V.D.I. Zeitung* **77**, 318.
- SCHMEECKLE, M.W. 2014 Numerical simulation of turbulence and sediment transport of medium sand. *J. Geophys. Res.* **119** (6), 1240–1262.

Drag model of finite-sized particle in wall turbulence

- SCHNEIDERS, L., MEINKE, M. & SCHRÖDER, W. 2017 Direct particle–fluid simulation of Kolmogorov-length-scale size particles in decaying isotropic turbulence. *J. Fluid Mech.* **819**, 188–227.
- SEMINARA, G. 2010 Fluvial sedimentary patterns. *Annu. Rev. Fluid Mech.* **42** (1), 43–66.
- SEYED-AHMADI, A. & WACHS, A. 2020 Microstructure-informed probability-driven point-particle model for hydrodynamic forces and torques in particle-laden flows. *J. Fluid Mech.* **900**, A21.
- STOKES, G.G. 1851 On the effect of the internal friction of fluids on the motion of pendulums. *Trans. Camb. Phil. Soc.* **9**, 8–106.
- TANAKA, M. 2017 Effect of gravity on the development of homogeneous shear turbulence laden with finite-size particles. *J. Turbul.* **18** (12), 1144–1179.
- TANAKA, M. & TERAMOTO, D. 2015 Modulation of homogeneous shear turbulence laden with finite-size particles. *J. Turbul.* **16** (10), 979–1010.
- TANG, Y., PETERS, E.A.J.F. & KUIPERS, J.A.M. 2016 Direct numerical simulations of dynamic gas–solid suspensions. *AIChE J.* **62** (6), 1958–1969.
- TENNETI, S., GARG, R. & SUBRAMANIAM, S. 2011 Drag law for monodisperse gas–solid systems using particle-resolved direct numerical simulation of flow past fixed assemblies of spheres. *Intl J. Multiphase Flow* **37** (9), 1072–1092.
- UHLMANN, M. 2005 An immersed boundary method with direct forcing for the simulation of particulate flows. *J. Comput. Phys.* **209** (2), 448–476.
- VASSEUR, P. & COX, R.G. 1977 The lateral migration of spherical particles sedimenting in a stagnant bounded fluid. *J. Fluid Mech.* **80** (3), 561–591.
- WANG, P., FENG, S.J., ZHENG, X.J. & SUNG, H.J. 2019 The scale characteristics and formation mechanism of aeolian sand streamers based on large eddy simulation. *J. Geophys. Res.* **124** (21), 11372–11388.
- WANG, Y.Q., ZHU, Z.P., HU, R.F. & SHEN, L. 2022 Direct numerical simulation of a stationary spherical particle in fluctuating inflows. *AIP Adv.* **12** (2), 025019.
- WATANABE, H. 1989 Drag coefficient and voidage function on fluid-flow through granular packed-beds. *Intl J. Engng Fluid Mech.* **2** (1), 93–108.
- WIBERG, P.L. & SMITH, J.D. 1985 A theoretical model for saltating grains in water. *J. Geophys. Res.* **90** (C4), 7341–7354.
- WU, Y., WANG, H.F., LIU, Z.H., LI, J., ZHANG, L.Q. & ZHENG, C.G. 2006 Experimental investigation on turbulence modification in a horizontal channel flow at relatively low mass loading. *Acta Mechanica Sin.* **22** (2), 99–108.
- YEO, K., DONG, S., CLIMENT, E. & MAXEY, M.R. 2010 Modulation of homogeneous turbulence seeded with finite size bubbles or particles. *Intl J. Multiphase Flow* **36** (3), 221–233.
- YOUSEFI, A., ARDEKANI, M.N. & BRANDT, L. 2020 Modulation of turbulence by finite-size particles in statistically steady-state homogeneous shear turbulence. *J. Fluid Mech.* **899**, A19.
- YOUSEFI, A., ARDEKANI, M.N., PICANO, F. & BRANDT, L. 2021 Regimes of heat transfer in finite-size particle suspensions. *Intl J. Heat Mass Transfer* **177**, 121514.
- YU, Z.S., LIN, Z.W., SHAO, X.M. & WANG, L.P. 2017 Effects of particle-fluid density ratio on the interactions between the turbulent channel flow and finite-size particles. *Phys. Rev. E* **96** (3), 033102.
- ZENG, L.Y., BALACHANDAR, S., FISCHER, P. & NAJJAR, F. 2008 Interactions of a stationary finite-sized particle with wall turbulence. *J. Fluid Mech.* **594**, 271–305.
- ZENG, L.Y., NAJJAR, F., BALACHANDAR, S. & FISCHER, P. 2009 Forces on a finite-sized particle located close to a wall in a linear shear flow. *Phys. Fluids* **21** (3), 033302.
- ZHAO, L.H., ANDERSSON, H.I. & GILLISSEN, J.J.J. 2010 Turbulence modulation and drag reduction by spherical particles. *Phys. Fluids* **22** (8), 081702.
- ZHAO, L.H., ANDERSSON, H.I. & GILLISSEN, J.J.J. 2013 Interphasial energy transfer and particle dissipation in particle-laden wall turbulence. *J. Fluid Mech.* **715**, 32–59.
- ZHENG, X.J. 2009 *Mechanics of Wind-Blown Sand Movements*. Springer Science & Business Media.
- ZHENG, X.J., FENG, S.J. & WANG, P. 2021 Modulation of turbulence by saltating particles on erodible bed surface. *J. Fluid Mech.* **918**, A16.
- ZHENG, X.J., JIN, T. & WANG, P. 2020 The influence of surface stress fluctuation on saltation sand transport around threshold. *J. Geophys. Res.* **125** (5), e2019JF005246.
- ZHOU, Q. & FAN, L.S. 2014 A second-order accurate immersed boundary-lattice Boltzmann method for particle-laden flows. *J. Comput. Phys.* **268**, 269–301.
- ZHOU, Q. & FAN, L.S. 2015 Direct numerical simulation of moderate-Reynolds-number flow past arrays of rotating spheres. *Phys. Fluids* **27** (7), 073306.
- ZHU, Z.P., HU, R.F., LEI, Y.H.N., SHEN, L. & ZHENG, X.J. 2022 Particle resolved simulation of sediment transport by a hybrid parallel approach. *Intl J. Multiphase Flow* **152**, 104072.